The Cryosphere, 20, 6423–6452, 2026
https://doi.org/10.5194/tc-20-6423-2026
© Author(s) 2026. This work is distributed under
the Creative Commons Attribution 4.0 License.

The Cryosphere Open Access EGU

Summer subsurface temperature variability in the percolation zone of southwest Greenland: high resolution observations of the top meter of firn

Anne Sledd[1,2], Michael R. Gallagher[1,2], Matthew D. Shupe[1,2], Christopher J. Cox[2], Robert Hawley[3], Michael S. Town[4], Heather Guy[5,6], Hans-Peter Marshall[7], Ryan R. Neely III[5,6], Claire Pettersen[8], Von P. Walden[9], Catherine Hebson[9], Andrew Martin[5,6], Erik Olson[10], and Derek Pickell[3]

[1]Cooperative Institute for Research in Environmental Sciences, University of Colorado Boulder, Boulder, CO, USA
[2]National Oceanic and Atmospheric Administration Physical Sciences Laboratory, Boulder, CO, USA
[3]Department of Earth Sciences, Dartmouth College, Hanover, NH, USA
[4]Earth and Space Research, Seattle, WA, USA
[5]National Centre for Atmospheric Science, Leeds, UK
[6]School of Earth, Environment and Sustainability, University of Leeds, Leeds, UK
[7]Department of Geosciences, Boise State University, Boise, ID, USA
[8]Climate and Space Sciences and, Engineering, University of Michigan, Ann Arbor, MI, USA
[9]Department of Civil and Environmental Engineering, Washington State University, Pullman, WA, USA
[10]Space Science and Engineering Center, University of Wisconsin-Madison, Madison, WI, USA

Correspondence: Anne Sledd (anne.sledd@colorado.edu)

Received: 1 April 2026 – Discussion started: 16 April 2026
Revised: 9 August 2026 – Accepted: 16 September 2026 – Published: 11 November 2026

Abstract. As surface melt affects larger areas of the Greenland Ice Sheet, quantifying the energetic processes governing the near-surface firn becomes increasingly important. This work characterizes subsurface temperature and its temporal variability in the upper meter of firn in the percolation zone in southwest Greenland from two months of observations in summer 2024. We provide novel methods for identifying the snow surface height from high resolution (2 cm and 15 min) temperature string measurements and further correct the observations for apparent biases from solar heating. Using these observations, we identify several thermodynamic layers relative to the surface. The rapid-response layer is the upper few centimeters of firn or snow where subsurface temperature is highly correlated (> 0.9) with skin temperature due to coupling with the atmosphere and absorption of incoming solar radiation. In the diurnally-responsive layer, temperature still responds to atmospheric variability with large positive and negative vertical and temporal temperature gradients, down to approximately 35 cm below the surface. Below the diurnally-responsive layer, the firn response to seasonal warming becomes decoupled from diurnal- and synoptic-scale atmospheric variability with depth; beneath 65 cm below the surface, correlations are less than 0.1 between subsurface temperature and skin temperature. While conduction slowly transports energy below the diurnally-responsive layer, surface melt and the advection of meltwater or latent heat can move relatively large amounts of energy that cause complex temperature gradients. Our results highlight both the value of high-resolution observations for understanding energy transfer in the near-surface firn and the need for additional observations.

1 Introduction

Under a warming climate, an increased area of the Greenland Ice Sheet (GrIS) is melting (Mottram et al., 2019). Given that at least 50 % of the contemporary GrIS mass loss is from changes in the surface forcing (The IMBIE Team, 2020), it is increasingly important to understand the energetics that drive

melt at the surface (e.g., Van Den Broeke et al., 2016; Zheng et al., 2025). Within the accumulation zone of the GrIS more area is projected to transition from the dry snow zone, where there is little to no melt, to the percolation zone, where melt occurs and may runoff or be retained in the firn (McGrath et al., 2013). Regions of the current percolation zone are also experiencing more melt, and higher elevations are contributing to runoff (Van Angelen et al., 2014; Tedstone and Machguth, 2022). These findings collectively underscore the importance of evaluating energy exchange processes responsible for surface melt in the percolation zone.

The near-surface firn, compacted snow that has survived a melt season, and younger snow above it are effectively an interface layer that modulates the exchange of energy between the atmosphere and deeper firn. For simplicity, throughout this paper we refer to the entire near-surface firn-snow column simply as firn. The upper tens of centimeters of firn have a diurnal cycle partially driven by solar absorption (Pfeffer and Humphrey, 1996; Kuipers Munneke et al., 2009). Ventilation can also impact temperature changes in firn given its porosity (Albert and Mcgilvary, 1992; Colbeck, 1997). Latent heat release from meltwater refreezing warms firn (e.g., Pfeffer and Humphrey, 1996; Covi et al., 2023), and both latent heat release and conduction contribute to heat uptake in firn further below (Saito et al., 2024).

"Near-surface" in many of these studies refers to the upper ~ 10 m of firn and often does not resolve the uppermost layers of firn at the snow-atmosphere interface. Part of the neglect of the upper meter of firn has to do with limitations of temperature observations in firn. For instance, temperature sensors near the surface are known to experience preferential heating from solar radiation (e.g., Pfeffer and Humphrey, 1996; Humphrey et al., 2012; Samimi et al., 2020). Observation-based studies of firn temperature are also limited by vertical resolution. While there are some datasets with higher resolution temperature profiles (Pfeffer and Humphrey, 1996; Dadic et al., 2008; Humphrey et al., 2012; Samimi et al., 2020; Guy et al., 2023), most measurements of firn temperature across the GrIS have vertical resolution of 50–100 cm (e.g., Fausto et al., 2021). These lower resolution observations are sufficient for studying energy exchange in firn across the seasonally active layer and below (e.g., Humphrey et al., 2012), but they are insufficient to resolve temperature gradients within the upper meter of firn related to diurnal and synoptic variability of atmospheric forcing. Without adequate observations, assessments of the upper firn commonly use surface energy balance and firn models forced at the boundaries with observations of the lower atmosphere from autonomous weather stations (e.g., Van Den Broeke et al., 2011; Vandecrux et al., 2018), sometimes utilizing temperatures from thermistor strings when available (e.g., Hills et al., 2018). The high resolution temperature datasets from the percolation zone (Humphrey et al., 2012; Samimi et al., 2020) were used to study meltwater but not energetic processes.

Novel measurements from an autonomous research platform installed near the DYE-2 site and Raven skiway in Greenland (Fig. 1) during May–August 2024 (Gallagher et al., 2026a) provide an opportunity to examine such energetic processes in the upper firn. This platform was part of a lower elevation expansion of the Integrated Characterization of Energy, Clouds, Atmospheric State, and Precipitation at Summit (ICECAPS) program (Shupe et al., 2013). These observations were targeted at the percolation zone of the southwestern GrIS, an area that has experienced some of the most rapidly increasing melt rates in Greenland (Zheng et al., 2025). The deployment included detailed measurements of atmospheric fluxes, meteorological parameters, clouds, and precipitation. In this work we focus primarily on the highly-resolved observations of temperature in the upper ~ 1 m of firn that serves as an interface between the atmosphere and ice sheet.

The goal of this work is to characterize high resolution temperature profiles and energetic drivers in the upper meter of firn that have received limited attention from previous observations in the percolation zone. To support this goal, we first develop methods for processing and correcting high-resolution temperature observations during the observational period of May through July. From these observations, we find enhanced temperature variability in the uppermost centimeters of firn due to atmospheric variability that decays with depth and is complicated by melt and refreeze. We further quantify energetic fluxes in the subsurface to understand the partitioning of energy accumulation, which highlights both limitations of the observations and opportunities for future improvements.

2 Data and methods

2.1 Field location and instrumentation

The summer 2024 deployment was an autonomous, pilot extension project of the ICECAPS observatory at Summit (Shupe et al., 2013). The installation site was near the Raven skiway and DYE-2 site at 66.48° N, 46.30° W, and 2094 m above sea level, approximately 140 km from the ice edge (Fig. 1a). Samimi et al. (2021) estimated DYE-2 to experience an average of 28 melt days during the summer, but the summer of 2024 was colder and snowier than average across the GrIS (Poinar et al., 2025).

The instrument platform consisted of a suite of complementary measurements installed on and around a skid-borne frame structure collectively called the Cryosphere, Atmosphere, Mass and Energy Observatory (CAMEO). Radiative fluxes were measured at 2 m above the surface using paired upward- and downward-facing broadband pyranometers and pyrgeometers, plus an upward-facing pyranometer for simultaneously measuring direct and diffuse shortwave radiation components. The surface brightness temperature was

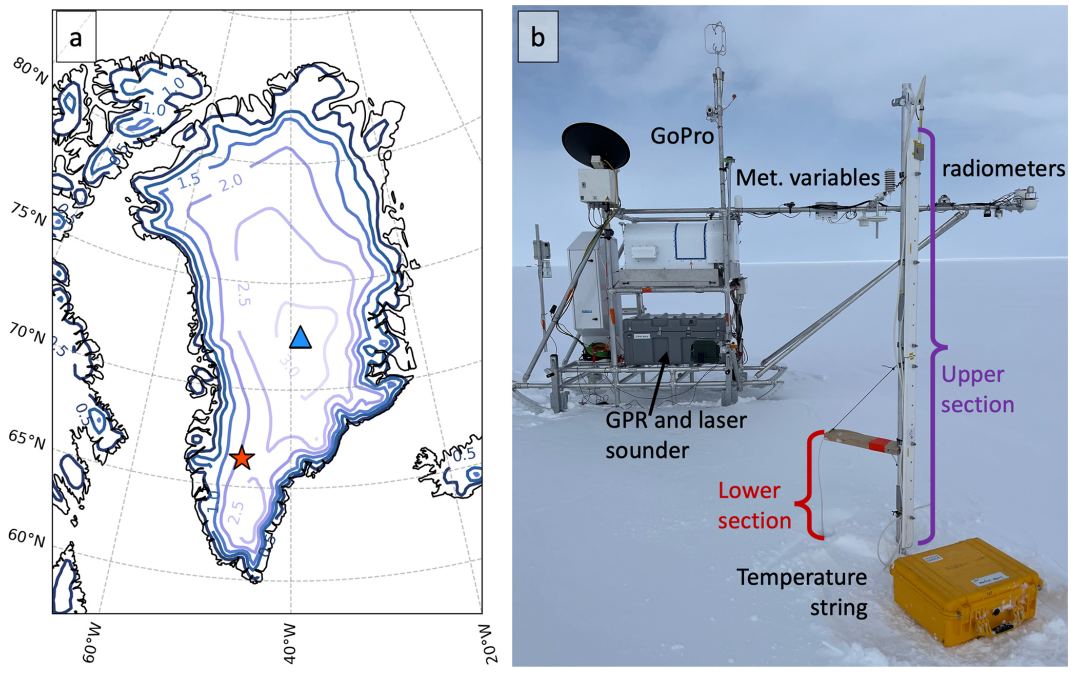


Figure 1. (a) Locations of observations used in this study in the percolation zone (red star) and Summit Station (blue triangle). Colored contour lines show elevation in kilometers. **(b)** Instruments used from the autonomous measurement platform collectively called the Cryosphere, Atmosphere, Mass and Energy Observatory (CAMEO). Photo credit: Matthew Shupe.

measured using a downward-pointing infrared thermometer. Meteorological variables, including a shielded temperature sensor, were measured at 2 m height, while winds were measured using a three-dimensional sonic anemometer at 3.8 m height. Surface height variations were measured by multiple instruments including an acoustic sounder, a laser sounder, and multiple GNSS receivers mounted on and around CAMEO. A Ground Penetrating Radar (GPR) operated at center frequencies of 5.4 and 7.7 GHz was used to identify times when liquid water was present within the firn based on signal attenuation (see Gallagher et al., 2026b). Firn temperature profiles were measured at 2 cm vertical and 15 min temporal resolution using a temperature string with digital sensors installed approximately 3 m away from CAMEO. A vertical, 5 cm wide hole was drilled in the firn and backfilled with granulated snow after the temperature string was inserted to a depth of $\sim$ 120 cm. A loop in the temperature string near the surface allowed for the sub-surface measurements to be horizontally separated from the support infrastructure, but required a dedicated data merging approach (see Appendix C). Ice lenses were identified at some depths adjacent to the temperature string when it was removed at the end of the measurement period. Two snow pits were dug 2–3 and $\sim$ 20 m from CAMEO during installation, and one snow pit was dug between CAMEO and the temperature string during decommissioning. Snow pits were approximately 1–1.5 m deep and included manual density measurements, capacitance based density measurements (Denoth, 1989; Wolfspeger et al., 2023), and layer identifications (Town et al., 2026). For use here, atmospheric observations (e.g., radiative fluxes, skin temperature, wind) are averaged to 10 min resolution and interpolated to temperature string time steps. Instruments used, their uncertainties, and descriptions of their spatial footprints are listed in Appendix A.

Skin temperature, ($T_{\mathrm{skin,rad}}$), serves as an independent measure of the surface temperature to validate the temperature string methods in Sect. 2.2. $T_{\mathrm{skin,rad}}$ is calculated from up- and downwelling longwave radiation after the upwelling longwave flux has been corrected for an apparent solar bias, detailed in Appendix B.

2.2 Enabling high resolution subsurface temperature observations

To evaluate energetic processes of the near-surface firn, the temperature string data must be processed and corrected. While some of this processing is specific to the instrument setup for this campaign, other processing steps are likely applicable to temperature string measurements more broadly. First we concatenate the upper and lower sections of the temperature string (Fig. 1b) because over the observation period the lower section of the temperature string was entirely buried by fresh snow (see details in Appendix C). Next we remove and interpolate temperature data that was impacted by shading of the temperature string. We then develop an algorithm to make a first guess of the firn surface height from the

temperature profiles. This surface height estimate is needed for the next step of correcting solar heating of the temperature sensors because the amount of solar radiation incident on sensors depends on their depth below the surface. Through optimization of the solar heating correction we further refine the surface height. These more general temperature string processing steps are explained below.

2.2.1 Temperature string solar shading adjustment

The support structure of the temperature string (a $\sim$5 cm diameter aluminum pole with mount plate) shaded its lower section at certain angles of direct shortwave radiation (Fig. D1a). This shading caused decreases in temperature around 15:00 (all times are in UTC) that do not agree with $T_{\text{skin,rad}}$ (Fig. D1b). Because this shading is not representative of the surrounding snow conditions, we remove impacted temperatures and interpolate temporally. This adjustment is performed on 14 d that experience significant direct incoming solar radiation rather than days with primarily diffuse radiation, defined as when the diffuse fraction is less than 0.5 between 10:00–17:00. A curve is fit to the time series of temperature from each height from 46 cm (the highest level used from the lower temperature string section) to -40 cm (Fig. D1c). This shading adjustment represents a minimum of the solar heating since there will still be diffuse light in the snow pack from the surrounding unshaded snow. At the lowest levels any changes in temperature from this interpolation are within the instrument uncertainty. Most of the adjustment is within the upper 20 cm of snow (Fig. 2a), consistent with past observations (e.g., Brandt and Warren, 1993).

2.2.2 Surface detection from high resolution firn temperature profiles

Although there was a suite of sensors installed on site to detect surface height changes, they differ by tens of centimeters at times due to spatial variability of snow distribution and all are approximately 3 m or more away from the temperature string. Because greater precision is needed to study the near-surface firn, we estimate the surface locally using the data from the temperature string. The approach takes advantage of the fact that the thermal properties of snow differ from those of air, which has been previously used to identify air-snow interfaces (e.g., Zuo et al., 2018). For this purpose, the vertical temperature gradient, $\Delta T/\Delta z$, is calculated at each time step using centered differencing (Fig. 3a). A running temporal variance of this gradient is calculated in 24 h centered windows (Fig. 3b). Some levels are manually excluded to enhance the surface, including when there is evidence of lateral transport of melt water below the surface. Levels that are 40 cm above the surface at installation are also excluded before 27 June 2024 since the support structure can impact the vertical gradient. At each timestep, the profile of variance is normalized vertically, and the first estimate of the surface is identified as the height with maximum variance in the profile (Fig. 3c). We further build on this algorithm when correcting for solar heating of the temperature string. Given that the amount of solar radiation penetrating the firn to the temperature string depends on where the surface is, we use the solar correction method (discussed next) to further refine the surface location. The resulting $+4$ cm offset is applied to all timesteps and improves agreement with the manual measurement of the surface height from the decommissioning in August. Using a 24 h interval for calculating the variance means that any rapid changes to the surface height may not be well represented. However, a longer interval is needed because the diurnal cycle of $\Delta T/\Delta z$ is what drives the maximum variance.

The temperature string surface height determined by this algorithm is within the range of independent surface height measurements (Fig. 3d). The temperature string surface height detection algorithm has some instances of the surface height temporarily decreasing more than other surface observations (e.g., 6 July). This difference could be an issue with the $\Delta T/\Delta z$ variance increasing because of advection of meltwater below the surface. However, the instrument and its support could also increase local melt, lowering the surface compared to nearby instruments, that is then preferentially filled in with drifting/blowing snow.

2.2.3 Solar heating correction for temperature string

There are temperature measurements greater than 0 °C below the surface from the temperature string that indicate the temperature string is absorbing more solar radiation than the surrounding firn (Fig. 3d). While past studies have acknowledged solar heating of temperature sensors (e.g., Brandt and Warren, 1993; Pfeffer and Humphrey, 1996; Samimi et al., 2020), we choose to correct, rather than ignore or remove, this bias because our focus is on near-surface temperature and gradient variability. To do so, our approach is to relate the temperatures above 0 °C below the surface to transmitted shortwave radiation (SWT) to create a correction proportional to SWT that is then applied for all time steps when SWT is greater than 0 W m^{-2}.

Because there were no observations of SWT in the snow or spectral SW measurements, we apply a methodology with assumptions commonly used by the snow community. First, we assume a fraction of net shortwave radiation (SWN) at the surface is in the near infrared (NIR), and that it is entirely absorbed between the surface and the first sensor below the surface (e.g., Warren, 1982). The remaining SWT is assumed to be in the visible range and absorbed exponentially with depth, z, (i.e., Beer's law) assuming a constant extinction coefficient, κ:

$$\text{SWT} = e^{-\kappa z}(1 - f)\text{SWN}. \quad (1)$$

The NIR fraction, f, and extinction coefficient were varied between 0.4–0.6 and 10–35 m^{-1}, respectively (Bohren

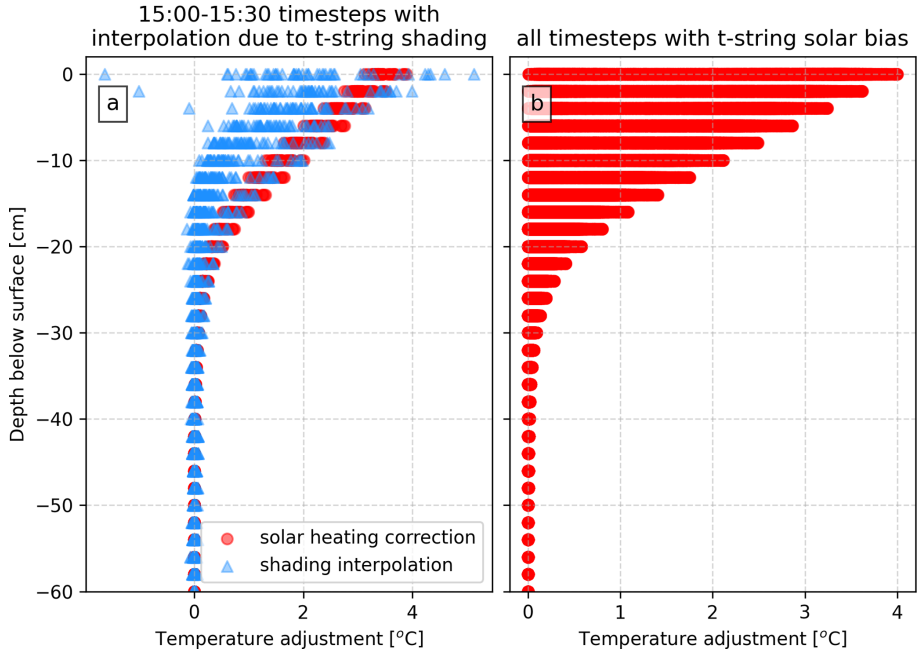


Figure 2. Magnitude of corrections applied to temperature string data. The differences between raw and interpolated temperature values from the shading adjustment (Sect. 2.2.1) are shown with blue triangles, and corrections due to solar heating of the temperature string (Sect. 2.2.3) are shown in red circles. In **(a)**, the plotted temperature adjustments are included only for timesteps that have the shading correction applied when the temperature string is fully shaded, i.e., days when the solar diffuse fraction is less than 0.5 between 15:00–15:30, for both the temperature string shading and solar heating adjustments. Shown in **(b)** are solar heating corrections for all timesteps they are applied. Shading the temperature string gives information about the depth of solar penetration in snow, so the general consistency between the solar bias correction (red circles) and adjustment due to shading (blue triangles) gives some confidence to the transmitted shortwave assumptions and the solar bias correction.

and Barkstrom, 1974; Mellor, 1977; Persson, 2012). Values of 0.5 and 19 m^{-1} were chosen to minimize both the number of temperature measurements above 0 °C and the difference between $T_{skin,rad}$ and the surface temperature from the temperature string ($T_{sfc,string}$) (Fig. 4a, b). Our optimized coefficients for SWT result in about 34 % of SWN being transmitted at least 2 cm below the surface. For comparison, Kuipers Munneke et al. (2009) found that 37 % of SWN was transmitted below 0.5 cm at Summit Station. As part of the temperature string correction, we regress temperature measurements above 0 °C that occur below the surface against the computed SWT at their depths.

In this correction, we also consider the possible impact of wind ventilation on temperature biases since snow is a porous medium that allows air movement below the surface (e.g., Colbeck, 1989; Albert and Mcgilvary, 1992). Given that the temperature string is positively biased compared to the surrounding snow, air movement could cause the temperature string to cool through sensible heat release. Therefore, we calculate a correction curve for three 2 m wind speed bins each with 33 % of the data. These wide wind speed bins are chosen due to limited sampling.

Within each wind speed bin, a curve is fit between temperature and SWT. SWT is divided into 20 bins for every 5th percentile. In each SWT bin, the median of the largest 15 % of data (black circles in Fig. 6a–c) is used to fit a correction curve (red triangles in Fig. 6a–c). We use this upper portion of the data because the temperature recorded by the temperature string above 0 °C is the minimum possible bias, but it could be larger if the firn is not melting. However, we use the median of the upper 15 % of data instead of the maximum value because we want to avoid overcorrection. The correction curves are inverse hyperbolic sine functions:

$$\text{temperature correction} = \text{arcsinh}^{-1}(\alpha \cdot \text{SWT}), \quad (2)$$

where α determines the steepness of the IHS curve. α is parameterized as a function of wind speed using α and the median wind speeds from each bin (Fig. 6d). Thus, the wind speed determines the slope of the IHS correction curve for a given timestep, and the temperature correction is then calculated using the IHS curve and SWT at each level below the surface. Wind speed was chosen as a parameter because of the expectation that given a temperature difference between the temperature string in the snow and the snow itself, higher wind speeds would more efficiently reduce the temperature difference through sensible heat transfer. However, this effect appears relatively limited with the maximum difference

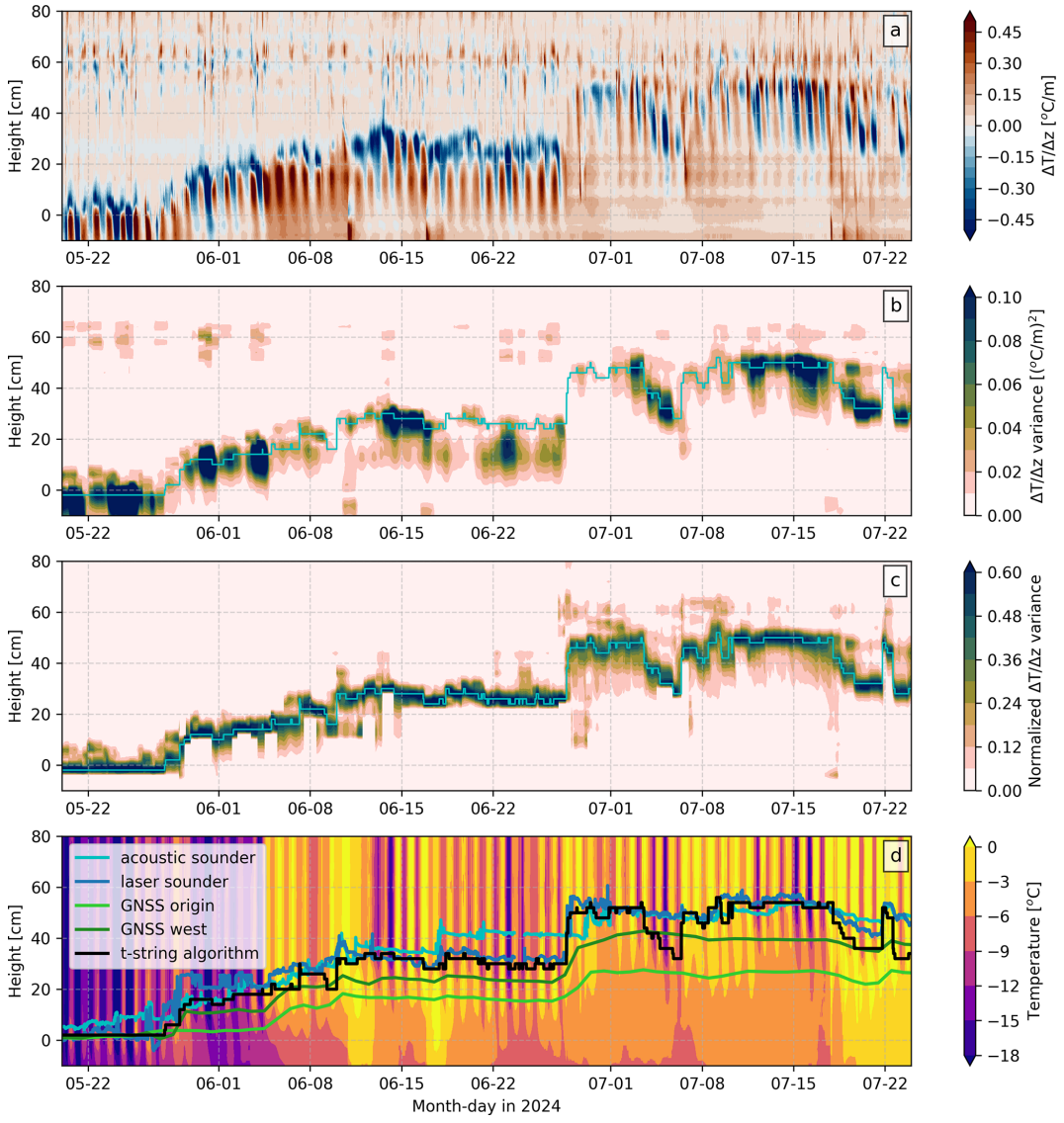


Figure 3. Surface height identification from the temperature string. **(a)** The vertical temperature gradient ($\Delta T/\Delta z$) is calculated at each 15 min time step using centered differencing. Positive (red) values are temperature decreases moving downward. **(b)** The variance of $\Delta T/\Delta z$ is calculated for a 24 h window for each timestep at each sensor level. **(c)** The $\Delta T/\Delta z$ variance shown in **(b)** is normalized vertically per time step. The cyan line is the maximum value of the normalized $\Delta T/\Delta z$ variance in each timestep. **(d)** Observations from the temperature string are plotted along with surface height estimates from the temperature string algorithm (black) and other surface height observations.

between high and low wind speed corrections on the order of 0.5 °C for large SWT (Fig. 6d).

The surface identified from the $\Delta T/\Delta z$ variance only, i.e., before adjusting with the +4 cm offset, is too warm compared to $T_{\text{skin,rad}}$ (Fig. 5a). This difference is especially notable at night, when no solar correction is applied. Adding an offset of +4 cm to the surface height improves the agreement between $T_{\text{skin,rad}}$ and $T_{\text{sfc,string}}$ (Fig. 5b). This adjustment is consistent with the idea that the identified surface is within the snowpack, where temperature changes are reduced compared to in the atmosphere. This discrepancy between surfaces is driven by the overall challenge in physically defining the surface of snow, given that it is a highly porous medium. The level at which different processes begin or end, i.e., solar radiation extinction, conduction, or convection, can define different interfaces, and will be discussed later in the results.

This methodology has a number of tunable parameters: the fraction of NIR absorbed near the surface; the visible extinction coefficient; the number of wind speed bins; what data are chosen to fit the correction curve; the magnitude of offset applied to the surface height estimate; and the choice of correction curve. These parameters are varied and tested against how many points below the surface have temperature above 0 °C; the difference between $T_{\text{sfc,string}}$ and the independent

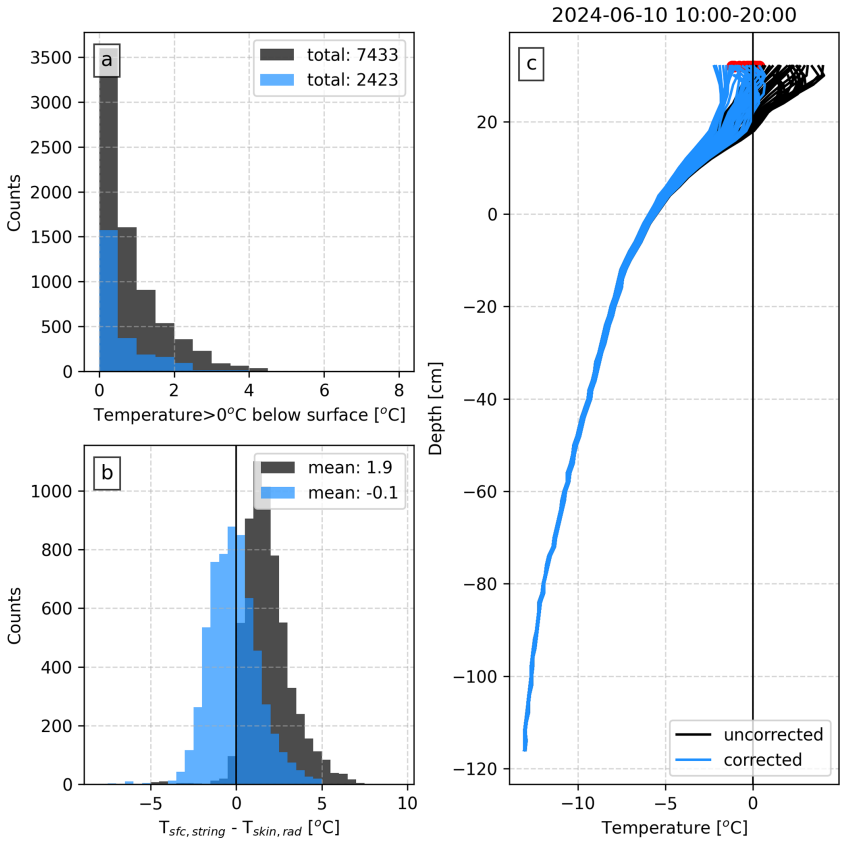


Figure 4. Comparison of solar heating corrected (blue) versus uncorrected (black) temperature from the temperature string. **(a)** Number of observations greater than 0 °C below the surface for all time steps. **(b)** Difference between surface temperature from the temperature string ($T_{\mathrm{sfc,string}}$) and radiometrically derived skin temperature ($T_{\mathrm{skin,rad}}$) for all time steps. **(c)** Temperature profiles from the temperature string with $T_{\mathrm{skin,rad}}$ values as red circles for 10 June 2024 10:00–20:00.

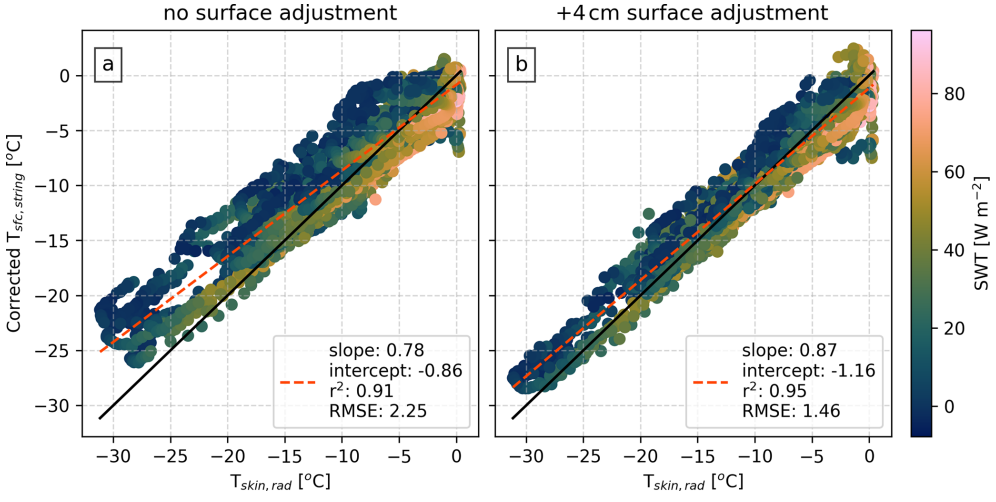


Figure 5. (a) Comparison of surface temperature from the temperature string ($T_{\mathrm{sfc,string}}$) and the radiometrically derived skin temperature ($T_{\mathrm{skin,rad}}$) for the surface identified in Fig. 3b, c and **(b)** with a +4 cm adjustment to the surface for all time steps colored by solar radiation transmitted below the surface (SWT). A 1 : 1 line is shown in black, and the best fit line using linear least-squares regression is shown with the dashed red line. The +4 cm also improves agreement between the temperature string algorithm surface height and manual measurements during instrument decommissioning.

$T_{\text{skin,rad}}$; and the profiles of temperature at timesteps where melt is likely (Fig. 4).

There are also a number of limitations to this correction, and the temperature string measurements, in general: the digital temperature sensors used in the temperature strings have suspected temperature-dependent bias (e.g., Sledd et al., 2024); the extinction coefficient should vary as a function of snow properties and/or presence of melt water (e.g., Perovich, 2007); the correction is determined from data when the surface is melting but applied to all times; NIR fraction could vary under clear or cloudy conditions; the results have a high dependence on the surface height identification, which is done with the uncorrected temperatures; and temperature string surface temperatures are still biased warm at night when there is no SWN. Many of these uncertainties are hard to quantify.

Despite these uncertainties, the solar heating correction improves how the subsurface temperature measurements compare to independent measurements of surface temperature. The number of temperature observations greater than 0 °C below the surface is reduced from ∼ 7500 to fewer than 2500 (Fig. 4a), and the mean difference between the $T_{\text{sfc,string}}$ and $T_{\text{skin,rad}}$ is −0.1 °C (Fig. 4b). There should still be some observations greater than 0 °C since there is instrument uncertainty for individual sensors. While there are no observations of SWT, the shading adjustment (Sect. 2.2.1) provides information on the depth and magnitude of solar absorption by the temperature string. The magnitude of the solar heating correction is similar to the shading adjustment below the surface (Fig. 2a). The heating correction, when limited to the same time steps as the shading adjustment, only follows the largest shading correction for a given depth. This may be due to the fact that the shading adjustment represents a minimum of the solar heating since there will still be diffuse light in the snow pack from the surrounding unshaded snow, or it could be a result of determining the solar bias correction when the surface is melting and the firn has different properties than when there is no melt. However, the overall agreement provides some confidence in the solar heating correction and assumptions used for it.

2.3 Subsurface flux calculations

Temperature changes both respond to and drive energy transport in firn; therefore, we outline our approximation of subsurface fluxes in this section. We calculate the change in internal energy, U, i.e., storage, over 20 cm thick layers at time, n:

$$U = \rho c_i \Delta z \frac{\delta T}{\delta t} = \frac{\rho c_i \Delta z \sum_{z=0}^{20\,\text{cm}} \left(T_{z,n+1} - T_{z,n-1}\right)}{(t_{n+1} - t_{n-1})}, \tag{3}$$

where c_i is heat capacity, T is temperature, t is time in seconds, and z is the vertical coordinate. The mean density, ρ, of each layer is calculated from manual measurements made during the installation and decommissioning of the instruments (Appendix A; Town et al., 2026) and linearly interpolated in time. Estimating step changes in density instead of linear trends slightly impacts the magnitude of fluxes over time but not the temporal variability or general conclusions of this work. New snow is assumed to have a mean density of 150 kg m^{-3} and standard deviation of 50 kg m^{-3}, which is within the range of measured surface density values. This assumption does not impact the main results. The layer thickness of 20 cm is chosen to account for uncertainty due to spatial variability, particularly the vertical distributions of ice lenses that differed between the snowpit and at the temperature string observed during the decommissioning. Conduction, FC, is calculated at the boundaries of each layer, e.g., −20 and −40 cm for a layer, as:

$$\text{FC} = -k \frac{\delta T}{\delta z}, \tag{4}$$

where the thermal conductivity, k, is calculated from density using Eq. (1) from Calonne et al. (2019). FC is defined as positive upward towards the surface. The net conduction into or out of a layer, ΔFC, is calculated as the difference between conduction at the top and bottom with positive values representing more energy conducted into the layer than leaving it. The absorption of SW in a layer, SWA, is given by

$$\text{SWA} = \left(1 - e^{-\kappa D}\right) \text{SWT}, \tag{5}$$

where D is the layer thickness, 20 cm. Taken altogether, the energy budget of each layer below the surface is described by:

$$\text{SWA} + \Delta\text{FC} + S = U. \tag{6}$$

S represents processes that are unaccounted for, such as the latent heat release from refreezing (a source) or sublimation (a sink). It also includes the uncertainty from all of the other terms. The terms in Eq. (6) are presented in Fig. D4 with S calculated as the residual. We do not calculate the residual for the top layer because it would require accounting for the atmospheric fluxes, which is beyond the scope of this work.

3 Results

In this section we first use the corrected temperature measurements to investigate temperature variability with time and depth for approximately the first month of observations to assess the transition from spring into the melt season. Next we quantify the temperature variability over the whole observed season, largely focusing on the average diurnal cycle with depth and key energetic processes. Finally, we shift perspectives to investigate how temperature variability impacts subsurface energy fluxes and the accumulation of energy in the subsurface over the melt season.

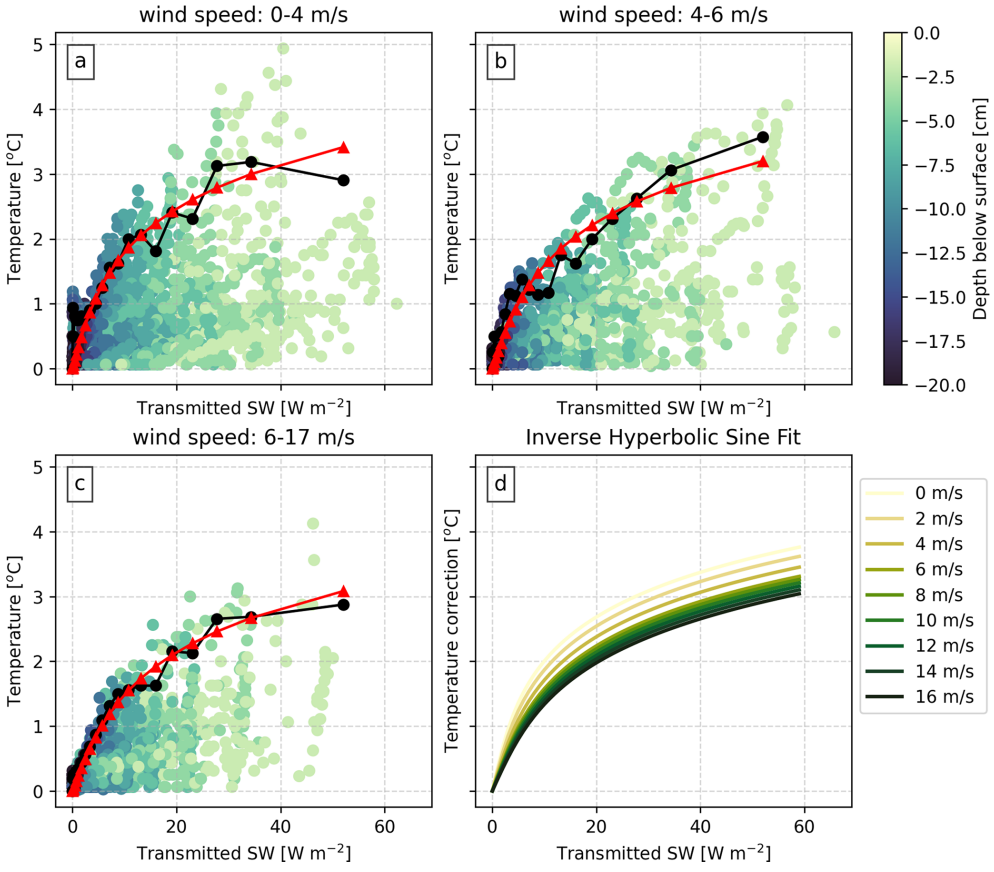


Figure 6. (a–c) Correction curves for solar heating of the temperature string within the firn for wind speed ranges given in the subtitles. Black circles are the upper 85th percentile of data for intervals of transmitted shortwave radiation (SW). The red curves with triangles are fitted using an inverse hyperbolic sine function. **(d)** The correction curve is parameterized based on **(a)–(c)**, so that at a given time step the wind speed determines the shape of the correction curve and the transmitted SW determines the magnitude of the correction.

3.1 Subsurface transition to melt

The first month of observations began with cold, dry conditions that transitioned to warming and eventually melt events. This progression is shown in profiles of temperature (Fig. 7c) and vertical (Fig. 7d) and temporal (Fig. 7e) gradients in the subsurface. For these temperature-related profiles, depth is in reference to the surface on 18 May when the temperature string was installed. $T_{\mathrm{sfc,string}}$ is compared to $T_{\mathrm{skin,rad}}$ in Fig. 7b, which also shows episodes of surface melt. Net longwave radiation is plotted in Fig. 7a to show the significant shifts in surface radiation related to atmospheric variability, and SWA is plotted in Fig. 7f. Recall that in our framework variability in SWA over time is due to differences in SWN only, and not due to any changes in optical properties of the snow, because we assume the extinction coefficient is constant in time.

In the first two weeks of observations, subsurface temperature primarily varies within the upper tens of centimeters in response to atmospheric variability. Before 5 June, $T_{\mathrm{sfc,string}}$ and $T_{\mathrm{skin,rad}}$ range from roughly −10 to −30 °C at night and −15 to −5 °C during the day (Fig. 7b), but below −50 cm, the temperature only varies from −15 to −12 °C (Fig. 7c). At −100 cm depth the temperature changes less than 1 °C over that time. Overall, $T_{\mathrm{sfc,string}}$ agrees with the magnitude and timing of the diurnal cycle of $T_{\mathrm{skin,rad}}$, with a +0.6 °C average difference and a root-mean-square error of 1.5 °C over this time period. The near-surface warming is coincident with the largest values of SWA, with roughly two thirds of SWN absorbed within 2 cm of the surface (Fig. 7f). The strongest temperature gradients also coincide with the largest SWA values, suggesting that increased temperature from SWA induces a temperature gradient and thus increases the conductive flux near the surface. The magnitude of warming in the uppermost firn is approximately twice as large as the cooling and extends further down, leading to the firn 20–50 cm below the surface warming by 3–5 °C by the end of May.

The first observed surface melt event occurs on June 5 after a series of warm days. Before this melt event, nighttime temperatures remain below −10 °C but were consistently above this temperature for multiple nights after, similar to the daytime temperatures in May. On the afternoon

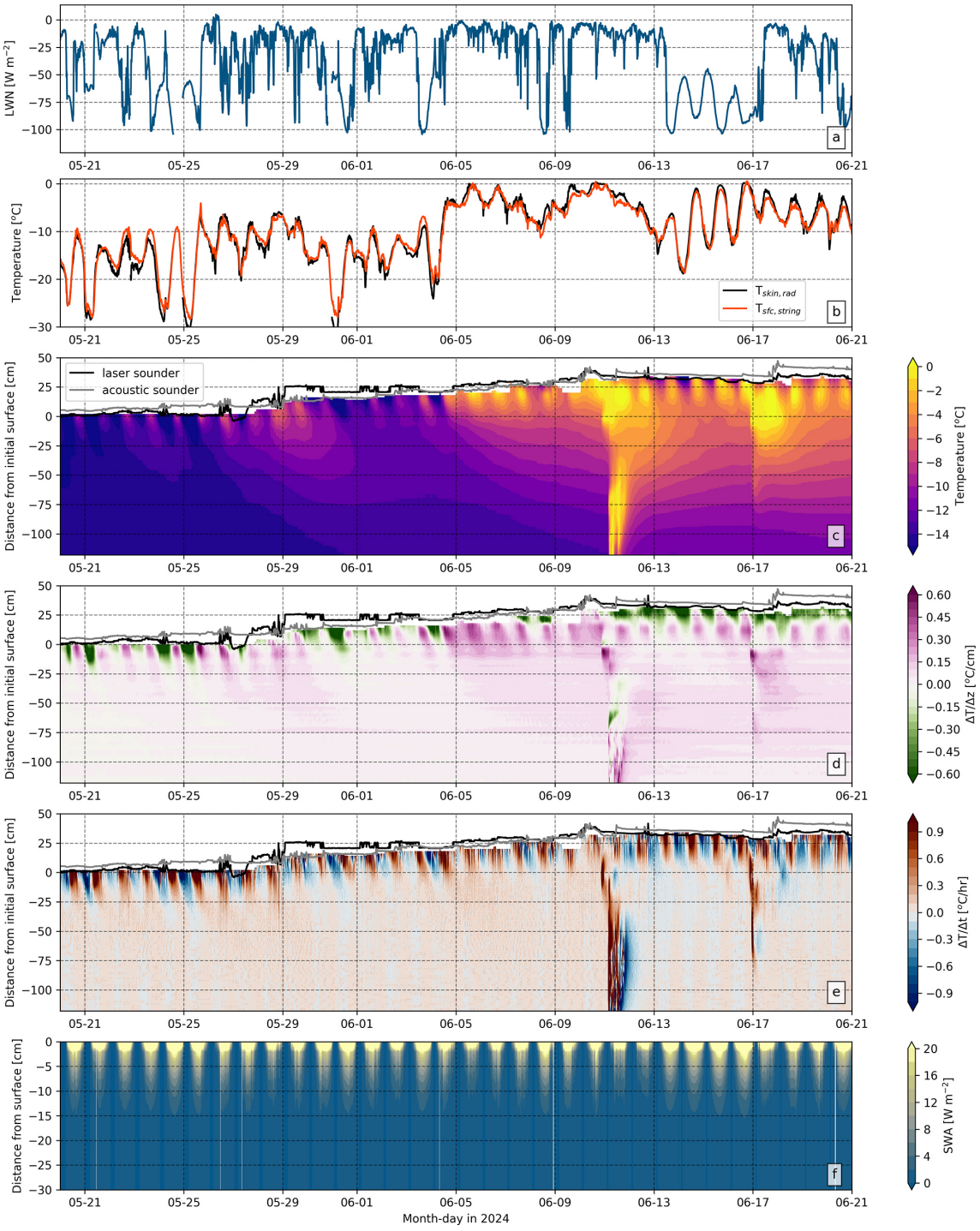


Figure 7. Observations of net longwave (LWN) **(a)**, surface temperature from the temperature string ($T_{\mathrm{sfc,string}}$) and radiometrically derived skin temperature ($T_{\mathrm{skin,rad}}$) **(b)**, temperature with depth **(c)**, vertical temperature gradient ($\Delta T/\Delta z$) **(d)**, temporal temperature gradient ($\Delta T/\Delta t$) **(e)** and absorbed solar radiation (SWA) **(f)**. Note the different y-limit in **(f)**. LWN values near $0\,\mathrm{Wm}^{-2}$ indicate radiatively cloudy conditions, and values around $-50\,\mathrm{Wm}^{-2}$ and lower indicate radiatively clear conditions. Temperature observations from the temperature string are only shown in the firn, meaning the white space in panels **(c)** through **(e)** is the atmosphere. Surface height observations from the acoustic and laser sounders are included for reference, but they are not expected to always agree with the surface identified from the temperature string.

of 5 June, $T_{\text{skin,rad}}$ and $T_{\text{sfc,string}}$ are both within uncertainty of 0 °C (Fig. 7b). Melt is confined to a shallow layer several centimeters near the surface because the temperature profiles show substantial remaining cold content below (Fig. 7c). Between 5–9 June, the upper 10 cm experiences less frequent and weaker cooling (Fig. 7e), and the vertical temperature gradient is almost always positive (Fig. 7d), indicating energy is continually conducting downwards from the relatively warm surface to colder firn below. After this event, depths below −10 cm warm by 1–3 °C.

Additional melt occurs in the following week, accompanied by the advection of meltwater that altered the subsurface temperature structure. Between 9–10 June there is melt during the day, and through the night $T_{\text{skin,rad}}$ remains above −2 °C due to persistent cloud cover, indicated by net longwave radiative fluxes greater than $-30\,\text{Wm}^{-2}$, which limits surface cooling (Fig. 7a–b). In addition to melt at and immediately below the surface, there is evidence of lateral movement of meltwater that creates a local temperature maximum, shown by the 0 °C temperature below −60 cm (Fig. 7c). While horizontal flow has been documented before (e.g., Humphrey et al., 2012), we suspect the support structure of the temperature string caused local downward channeling of meltwater that moved horizontally to the temperature string based on ice layers seen when removing the instrument at the end of summer (Fig. D2). Regardless of the exact origins of this meltwater, it alters the subsurface through the release of latent heat as it refreezes, such that the temperatures at those depths are never as cold as prior to this event and the entire observed firn column warms (Fig. 7c).

The latent heat from refreezing of this meltwater impacts the observed temperature structure over the following five days. At levels where liquid water was present, the surrounding firn warms as latent heat is released from the liquid water freezing. The increased temperature from liquid water/refreezing processes within cold firn at depth produces greater vertical temperature gradients away from the liquid water. These greater vertical temperature gradients indicate that there is increased conduction both upwards and downwards to conduct heat away from this source of latent heat (green and pink dipoles at 0 cm on 11 June and at −70 cm, relative to the initial surface, on 12 June in Fig. 7d), which are coincident with relatively large warming and cooling in time (Fig. 7e). As the atmosphere and skin temperature cool relative to the previous day, the subsurface remains warm and a negative (upward) vertical temperature gradient continually persists near the surface for the following two days (Fig. 7d). This phenomenon seems to be a consequence of latent heat release from freezing meltwater rather than from SWA since there is less SWN for the first two days after melt. This event highlights complexities of temperature gradients near the surface that would be excluded from lower resolution observations, particularly during melt and refreeze processes. While the surface location has some uncertainty, $T_{\text{sfc,string}}$ is in good agreement with $T_{\text{skin,rad}}$ during this period, and if the surface were below the negative $\Delta T/\Delta z$ values, $T_{\text{sfc,string}}$ would be larger than $T_{\text{skin,rad}}$. (Fig. 7b). Another melt event occurred 17 June with similar signatures of increased vertical and temporal temperature gradients near the surface with impacts down to −75 cm (Fig. 8d, e). Together, these events influence the seasonal temperature progression.

3.2 Subsurface temperature variability and its drivers

In this section we investigate the energetic signatures of the near-surface firn: how the temperature varies with depth and time aggregated over the whole season. To do so, we shift perspectives from considering temperature relative to the temperature string height, as in Fig. 7, to temperature relative to the surface (Fig. 8). Note that because the surface is always at 0 cm, any surface height change modifies the depth of observations throughout the column in Fig. 8a. This coordinate system highlights the (sub)surface relative to the atmosphere and allows us to quantify temperature variability (Fig. 8b), correlations with $T_{\text{skin,rad}}$ and $T_{\text{sfc,string}}$ (Fig. 8c), and warming trends over the season (Fig. 8d), all with depth relative to the surface. We explore the relevant processes by presenting diurnal cycles of temperature; vertical and temporal temperature gradients; and SWA, again with respect to the surface, in Fig. 9. Based on these temperature measurements, we identify and name notable thermodynamic layers in the upper meter of firn that respond to atmospheric variability on different time scales:

- Rapid-response layer: upper several centimeters of diurnally-responsive layer that respond in step with atmospheric variability; the most relevant processes in this layer include solar absorption and likely ventilation.

- Diurnally-responsive layer: the upper tens of centimeters that show changes in temperature and gradients over the diurnal cycle; the most relevant processes are solar absorption and conduction; this behavior has been noted in Greenland by Pfeffer and Humphrey (1996) and Kuipers Munneke et al. (2009).

- Seasonally-responsive layer: below approximately −60 cm where the firn is no longer instantaneously correlated with atmospheric variability but responds to seasonal warming; the most relevant process is conduction; essentially the seasonally active layer that extends down to a depth where there is no seasonal temperature change relative to the annual mean temperature (e.g., Colgan et al., 2018; Saito et al., 2024).

The specific depths for each layer are approximate and likely vary in time and space. Although we only name firn below −60 cm as the seasonally-responsive layer, the entire upper meter is traditionally considered part of the seasonally active layer that has a distinct annual temperature cycle. While melt and latent heat release also impact temperature

and gradients in all the layers, we do not label them as defining processes since melt is episodic in these observations and modulates typical energy exchange processes. Further details of the specific characteristics and processes that define and cause variability within these layers are discussed in the rest of this section.

The diurnally-responsive layer is most strongly coupled to atmospheric variability and experiences the largest warming on daily to seasonal timescales. SWA is concentrated near the surface and drives the rapid-response layer. Based on our calculations, there are fewer than 5 W m^{-2} of SWA absorbed below 10 cm at local solar noon (15:00), which is consistent with the maximum variability of temperature being largest at and just below the surface (Fig. 8b). The rapid-response layer has the largest standard deviation and highest correlation with $T_{\mathrm{skin,rad}}$ and $T_{\mathrm{sfc,string}}$ because it regularly experiences warming and cooling each day (Fig. 8b, c). Although nighttime $T_{\mathrm{sfc,string}}$ (blue line, Fig. 9b) is slightly higher than the average $T_{\mathrm{skin,rad}}$ over the same time period (blue triangle), there is overall good agreement between average $T_{\mathrm{sfc,string}}$ and $T_{\mathrm{skin,rad}}$. The nighttime minimum temperature extends down to around −15 cm, while the warming signature from the daytime persists down to −30 cm until 05:00 the following morning (Fig. 9a).

SWA alone cannot explain the depth of the diurnally-responsive layer because SWA is small below −10 cm, while temperature varies diurnally down to about −35 cm below the surface. Increased temperature near the surface from SWA can induce a temperature gradient that increases conduction further below the surface. The depth of the diurnally-responsive layer represents how far down the energy into the surface can be conducted until the diurnal temperature forcing near the surface shifts, which depends on how efficiently energy is conducted and the magnitude of the energy input. At the surface, the vertical temperature gradient is on average negative (green in Fig. 9c and black line in Fig. 9d), which implies that on average there was more energy being conducted upwards to the surface. This average negative vertical gradient at the surface is perhaps unexpected given an assumption of net energy into the surface, i.e., a positive gradient, to warm it and eventually cause melt during summer. Part of this result is due to the specific set of observed events, such as snowfall occurring after surface melt that insulated relatively warm temperatures, which are averaged together with occurrences of positive vertical temperature gradients (e.g., May dates in Fig. 7d). The average values reported in Fig. 9 also include melt at the surface, which has a distinct impact on vertical temperature gradients: because melting snow has an upper bound of 0 °C, the vertical temperature gradient goes to 0 °C cm^{-1} over the depth where snow is melting and the magnitude and frequency of downward $\Delta T/\Delta z$ is effectively truncated. Below this depth $\Delta T/\Delta z$ can increase to move the energy further down into the firn, and any percolation of meltwater will also warm the firn and release latent heat. If the surface refreezes while there is still liquid water below, energy can also be conducted upwards as the meltwater freezes at depth.

Further below the surface, the seasonal warming is driven by conduction with episodic contributions from latent heat release due to refreezing meltwater. Below approximately −20 cm, the temporal standard deviation of temperature decreases linearly, and the temperature below −1 m is about half as variable as the surface temperature (Fig. 8b). The linear decrease of temperature standard deviation with depth fits with conduction being linearly dependent on $\Delta T/\Delta z$, whereas the strongest variability at the surface corresponds to where $\Delta T/\Delta z$ and SWA are both large (Fig. 9d, h). The maximum $\Delta T/\Delta z$ during the day occurs at lower depths than the minimum $\Delta T/\Delta z$, indicating that daytime warming penetrates deeper than can be cooled at night, leading to a diurnal excess of energy that contributes to seasonal warming at depth (Fig. 8d). Below the diurnally-responsive layer, the average $\Delta T/\Delta z$ is weakly positive, meaning energy is conducted down into the firn over summer. This average also includes melt and refreeze events that cause relatively large vertical temperature gradients both upwards and downwards from a given level. However in these observations such events are not frequent enough to have a significant impact on the average $\Delta T/\Delta z$ at lower depths. The constant $\Delta T/\Delta z$ at depths below the diurnally-responsive layer is consistent with the rapid decline of correlation between surface temperature and the temperatures at depth (Fig. 8c). Below −60 cm the correlation is near zero, indicating that below this depth the firn no longer responds directly to changes from the atmosphere because its influence is dampened by the intervening firn.

The correlation between temperature at lower depths and the surface is also impacted by melt. The solid lines in Fig. 8b–c include the entire time series of temperature with depth, but the dashed lines exclude 11–12 June, when we suspect there was instrument-induced meltwater and horizontal advection and channeling to lower depths. This event increases the correlation between temperature below −60 cm and the surface because it warmed the firn at those levels around the same time that the surface warmed. Although this event had real impacts on the subsurface temperature, its magnitude and timing likely do not represent typical conditions or relationships between the subsurface and atmosphere. From both the full time series and the time series excluding that melt event, the correlations between the surface and temperature below approximately −60 cm are small.

While depths 50 cm below the surface warm approximately linearly, near the surface there is a complex interplay between the seasonal warming trend and the changing surface height. Figure 8d shows 4-week running means calculated at every 2 cm below the surface. These trends show that the diurnally-responsive layer in the upper 10–20 cm experiences the most variability and warming over the season compared to lower depths. The temperature variations, such as those around 2, 8, and 25 June, are due to increased surface

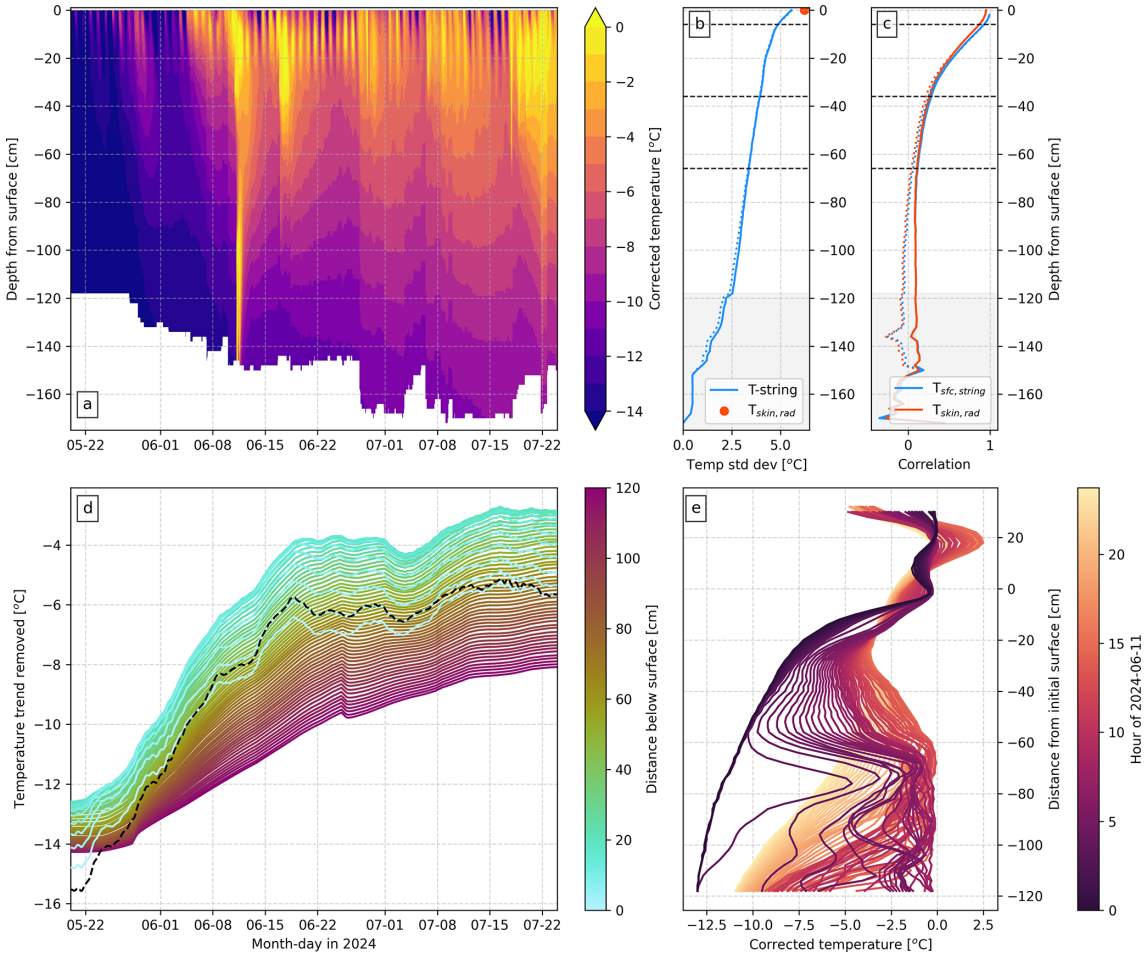


Figure 8. Temperature and its variability with respect to the surface. **(a)** Temperature profiles with depth adjusted so that the surface is always 0 cm. **(b)** Standard deviation of temperature over time from the temperature string (blue lines) and $T_{\mathrm{skin,rad}}$ (red circle). **(c)** Correlation between temperature at each depth below the surface and the surface temperature (depth = 0 cm) from the temperature string and $T_{\mathrm{skin,rad}}$. **(d)** 2-week running means of temperature from the temperature string (colored lines) at levels with a complete data record over the entire season and $T_{\mathrm{skin,rad}}$ (black dashed line). The running means in **(d)** are removed prior to calculating correlations in **(b)** and **(c)**. In **(b)** and **(c)**, dashed horizontal lines indicate the approximate lower levels of the rapid-response layer (−6 cm where the correlations are > 0.9), diurnally-responsive layer (−36 cm where temperature gradients have nearly zero diurnal variability), and the approximate upper level of the seasonally-responsive layer (−66 cm where the correlations are < 0.1). The grey shading below −116 cm in **(b)** and **(c)** indicates levels that have incomplete observations for the entire time period, which appears to impact the change of standard deviation and correlation with depth. **(e)** Temperature profiles observed during the melt event on 12 June 2024. The temperature in the middle of the profiles, roughly −20 to −60 cm relative to the initial surface height, do not reach 0 °C, indicating that meltwater did not channel down the entire temperature string but instead moved horizontally.

height from fresh snowfall that shifts the depth relative to the surface, as opposed to a sudden temperature warming caused by meltwater percolation or advection. There appears to be a maximum in mean warming below the surface compared to $T_{\mathrm{sfc,string}}$ or $T_{\mathrm{skin,rad}}$ trends, i.e., black dashed line vs teal 10 cm depth. This fact could be due to snowfall accumulation at the surface that lowers the surface temperature. Or, there could be more warming below the surface due to local temperature maxima from refreezing and latent heat release. It is possible these processes are even combined, such that fresh snowfall insulates the increased temperatures below the surface so those depths do not cool as efficiently as the surface, but they are difficult to disentangle with this set of observations.

3.3 Quantifying seasonal energy exchanges

Given the above processing and quality-assurance of the subsurface temperature measurements, we now use them to investigate how energy is distributed between different subsurface fluxes. By calculating SWA (Fig. D4a), change in internal energy (U; Fig. D4b), and difference in conduction

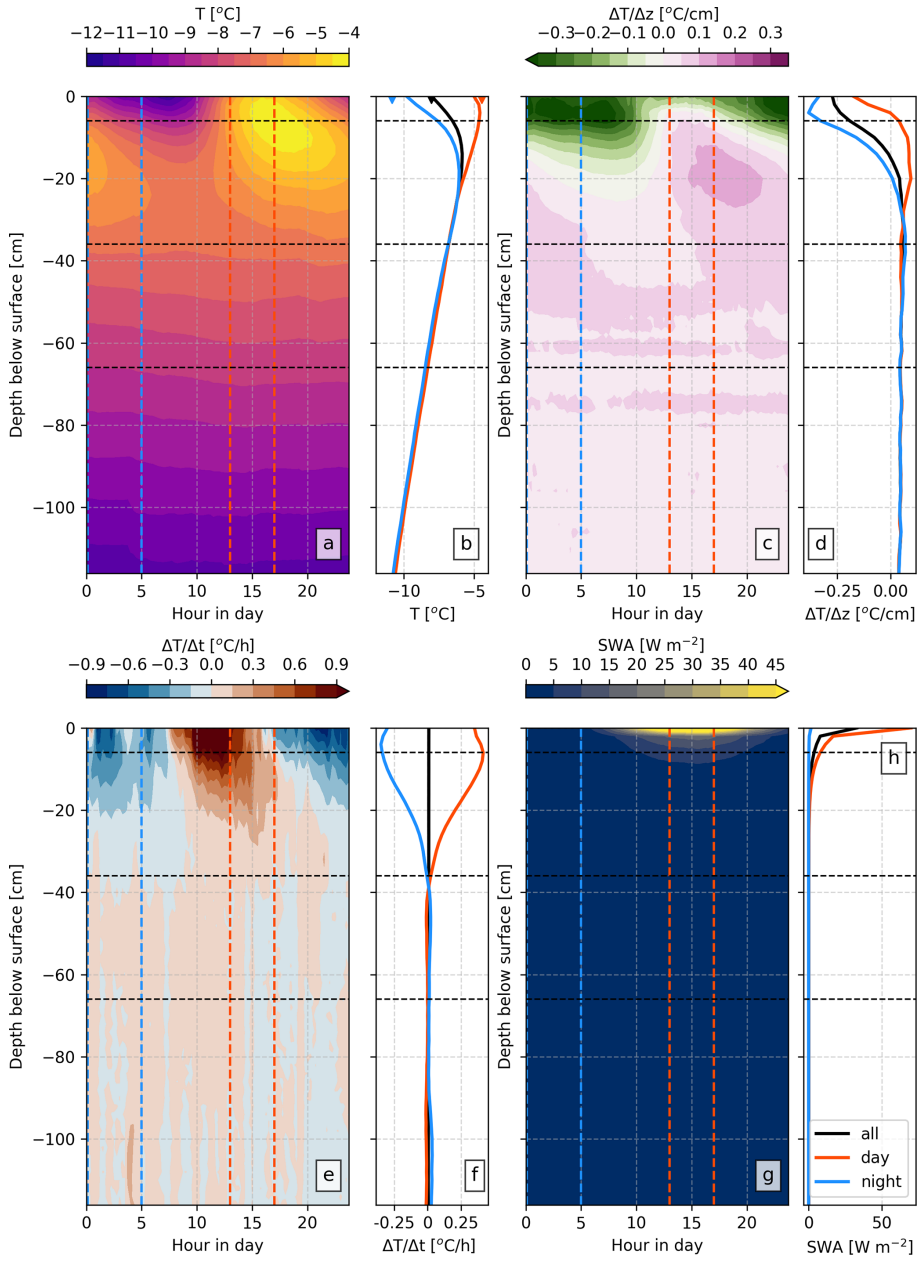


Figure 9. (a–b) Diurnal cycles and average profiles of temperature, **(c–d)** vertical temperature gradient ($\Delta T/\Delta z$), **(e–f)** temporal temperature gradient ($\Delta T/\Delta z$), and **(g–h)** absorbed shortwave radiation (SWA) calculated from all times. Average profiles are calculated over all hours ("all"/black), 00:00–5:00 ("night"/blue), and 12:00–15:00 ("day"/red). Triangles in **(b)** are averages calculated from $T_{\text{skin,rad}}$ over the same time subsets. Dashed horizontal lines indicate the approximate lower levels of the rapid-response layer (−6 cm where the correlations are > 0.9), diurnally-responsive layer (−36 cm where temperature gradients have nearly zero diurnal variability), and the approximate upper level of the seasonally-responsive layer (−66 cm where the correlations are < 0.1).

across the layer (Fig. D4d), we can solve for the residual using Eq. (6) and assess closure, with any residuals representing the energy associated with melt and refreeze (Fig. D4e). These fluxes are calculated for 20 cm thick layers, relative to the initial surface, rather than relative to the surface at each time steps as in the last section; only when the surface height is at or above 20 cm from the previous layer is a new layer included because the change in internal energy depends on thickness (Eq. 3). This criteria means layers above 0 cm only appear after 20 cm of snow has accumulated and that there can be gaps in the time series in Fig. 10 when the surface height is lowered during melt. The residual term is not calculated for layers at or near the surface. This exclusion is done because the atmospheric fluxes would need to be included

for closure of surface layers, which is the subject of ongoing work. "Surface layer" in this context refers to the full 20 cm layer that is at or closest to the surface at a given time. The time series of fluxes presented in Fig. D4 are further integrated in time so that each flux in Fig. 10 quantifies the total cumulative energy associated with each process over the observed time period, allowing us to assess the energy associated with different processes as the firn warms and responds to melt.

Nearly all SWA accumulates in the surface layer (Fig. 10a), which leads to a pattern of large energy accumulation in a given layer at the surface until it is buried under new snow. For example, the (0, −20) cm layer gains $\sim 36\,\mathrm{MJ\,m^{-2}}$ by 1 June. After the surface height increases in early June, SW is absorbed above this layer, and the cumulative SWA in the (0, −20) cm layer plateaus. This pattern repeats for the next surface layer, (20, 0) cm, from around 8 to 27 June. The surface layer also has the greatest variability of cumulative internal energy (Fig. 10b). While the (0, −20) cm layer is near the surface, cumulative internal energy changes vary from approximately -0.7 to $+0.5\,\mathrm{MJ\,m^{-2}}$ as SWA warms the snow and then the snow cools to the atmosphere. This rapid variability diminishes as new snow accumulates above the layer, and after the first week in June this layer changes internal energy like other subsurface layers: more gradually with net positive values. As with SWA, new surface layers show larger variability for cumulative internal energy that decays as the layer is buried under new snow.

In contrast to layers near the surface, lower layers show net positive cumulative internal energy, consistent with the subsurface warming over the summer (Fig. 10b). Cumulative changes in internal energy in subsurface layers are generally more gradual over time, with the exception of melt and advection events. The melt event on 11 June, discussed in Fig. 7, caused sharp, temporary increases in cumulative internal energy for layers at and below 0 cm. When the surface began melting, the upper firn was already relatively warm and then limited to 0 °C, so the change in internal energy over (20, 0) cm was similar to past variability. In contrast, changes in internal energy in subsurface layers were an order of magnitude larger because the firn was initially much colder, so the advection of liquid water caused a relatively large increase in internal energy, similar in magnitude to the rest of the seasonal cumulative warming in the subsurface by the end of July. The liquid water in these levels either froze or percolated further into the firn, and so the cooling firn manifests as a decrease in internal energy, albeit never to values as low as before the melt event. This pattern repeats itself on 17 June during another melt event.

For subsurface layers, there is net downward conduction because the firn at this time of year is generally colder with depth, excluding times with lateral transport of meltwater (Fig. 10c). For subsurface levels, the amount of cumulative conduction by the end of the season decreases with depth, by roughly half, since the temperature gradients decrease with depth (e.g., Fig. 7d). Levels at or near the surface have little to no cumulative conduction in comparison because the vertical temperature gradient changes sign with the diurnal cycle (e.g., Fig. 9c). Over (0, −20) cm there is initially a small positive (upward) cumulative conduction before 5 June, but once this layer is sufficiently buried by new snow, conduction begins a relatively steady negative (downward) trend. The additional surface layers deposited over time show net positive cumulative conduction by the end of the season, consistent with negative vertical temperature gradients at the surface, given that melt events earlier in the season warmed the firn relative to the new snow.

For layers that are always below the surface, i.e., (−20, −40) and below, the cumulative net conduction is either near zero or positive through the season, so conduction warms that layer of firn (Fig. 10d). Generally this process is steady with approximately linear increase over time. Again, the exceptions are melt or advection events when local temperature maxima create relatively large vertical temperature gradients, such as on 11 June, as in Fig. 7d. When a layer is at or near the surface, then cumulative net conduction is negative. For instance, cumulative net conduction for the (20, 0) cm layer is negative until there is another full layer above it, at which point the net change in cumulative conduction is zero or slightly positive. The (0, −20) cm layer shows a similar pattern until 1 July, after which there is a net loss of energy through conduction.

The sum of SWA, ΔFC, and internal energy should be zero in the absence of phase change and/or the advection of liquid water. Broadly, this expectation is met through mid-June in Fig. 10e. The sharp increases in the (0, −20) layer, which is near the surface, on 11 and 17 June are followed by plateaus of cumulative energy over 12–17 and 18–28 June that are consistent with the premise that the energy gained from melt and energy released as liquid water refreezes is transferred to lower layers via conduction. Lower layers show similar sharp increases in cumulative energy on 12 June, when it appeared there was horizontal advection of meltwater (Fig. 8e). However, these increases are followed by similarly sharp decreases, i.e., energy sinks, that could be explained by refreezing of the meltwater.

By the end of June, the high uncertainty in firn thermal properties limits meaningful interpretations of the cumulative residual energy in Fig. 10e. Several of the subsurface layers show gradual negative trends for cumulative energy beginning in the middle of June. According to Pfeffer and Humphrey (1996), apparent heat sinks at depth can occur when the actual thermal conductivity is lower than what is assumed, i.e., the calculated conductive flux leaving a layer is larger than the actual flux, making it appear that there is net energy lost. Apparent heat sources can also appear when the actual thermal conductivity is higher than what is assumed. Any such errors in the fluxes would also accumulate. The opposite could be true for the (0, −20) layer, which shows an increasing amount of cumulative energy that is not from

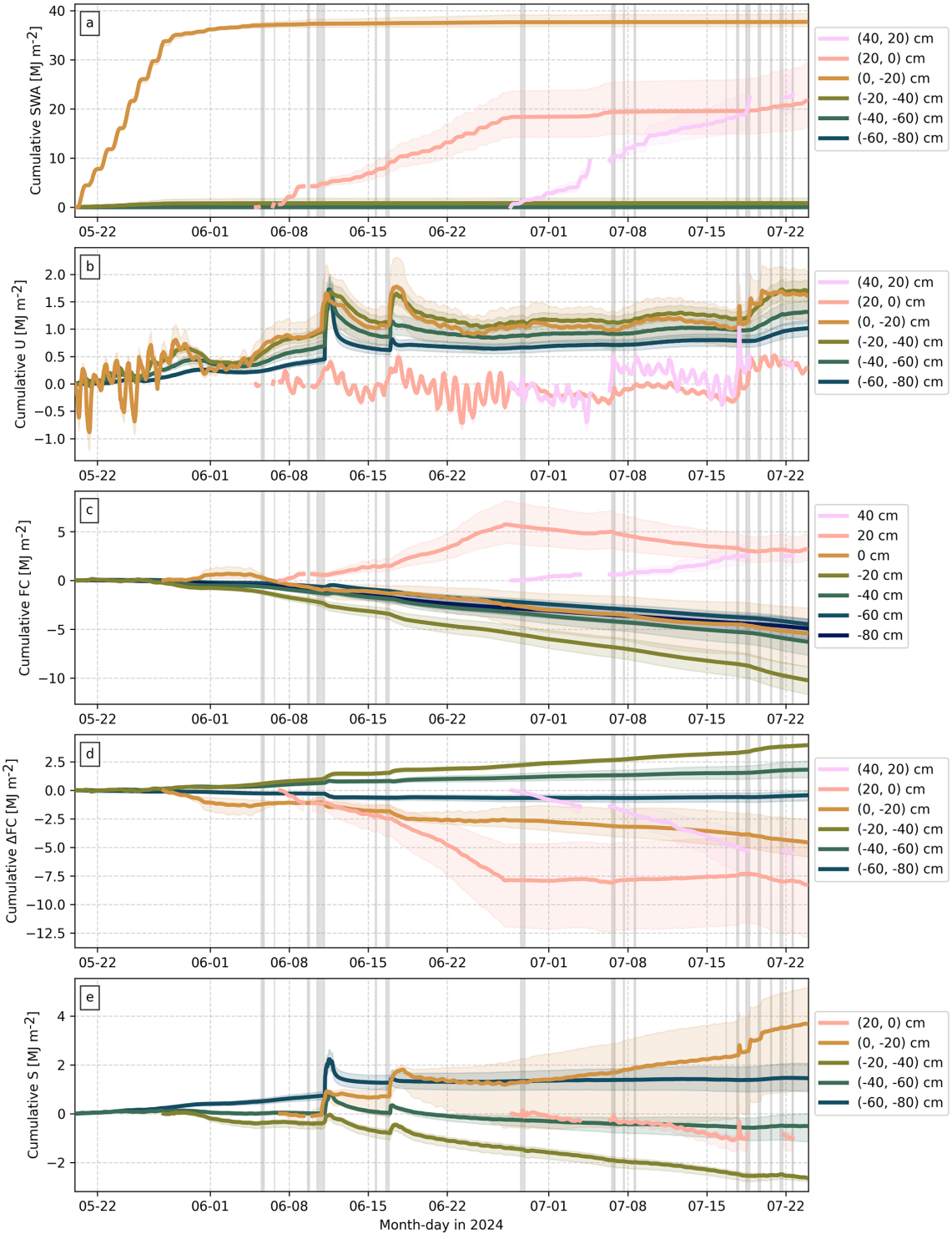


Figure 10. **(a)** Cumulative subsurface fluxes including absorbed solar radiation (SWA), **(b)** storage or change in internal energy (U), **(c)** conduction (FC), **(d)** the net conduction into or out of a layer (ΔFC), and **(e)** source terms calculated as the residual (S). Conduction is calculated at specified levels, and all other variables are calculated over 20 cm layers relative to the initial surface when instruments were installed. In **(a)**, the solid line is calculated assuming an extinction coefficient of $19\,\mathrm{m}^{-1}$, and the shading represents $\pm 20\,\%$ uncertainty in the extinction coefficient. For **(b–e)** the solid line is calculated using the mean density averaged over each layer, and the shading around lines for a given layer represents ± 1 standard deviation from density measurements within the layer boundaries, shown in Fig. S3. Vertical gray shading indicates times when $T_{\mathrm{skin,rad}} \sim 0\,^{\circ}\mathrm{C}$.

conduction or SWA, so the density, derived thermal conductivity, and conductive flux could be underestimated. Thermal conductivity is calculated using density from snowpits, which have their own uncertainty, measured at the beginning and end of the observations and linearly interpolated (see Fig. D3a, c). Assuming step changes for density, as opposed to linear, impacts the magnitude of cumulative storage and conduction but not the variability in time or general relationships of energy accumulation between layers (not shown).

4 Discussion and conclusions

Through this work we have created a set of high-resolution temperature observations from the upper meter of firn in the percolation zone of southwest Greenland in summer. The creation of the dataset requires methods for identifying the firn surface and correcting solar heating of the temperature string, and both techniques could be generally applied to other temperature string observations. Addressing these measurement complications, which have often caused near-surface firn temperature measurements to be ignored (e.g., Pfeffer and Humphrey, 1996; Dadic et al., 2008; Humphrey et al., 2012; Saito et al., 2024), was necessary for understanding energy variability in the near-surface firn. With the corrected observations, we identify key thermodynamic layers in the near-surface firn: the rapid-response layer in the uppermost few centimeters that is directly coupled to the atmosphere; the diurnally-responsive layer in the upper tens of centimeters that is driven by diurnal variability from the atmosphere; and a deeper seasonally-responsive layer that is decoupled from short-term atmospheric variability. The high vertical resolution of our observations is also crucial for evaluating the variability because more common coarsely resolved observations (e.g., 0.5 m vertical resolution) cannot resolve the impact of the atmosphere on these layers within the upper meter of firn.

The processes we have identified are consistent with past studies in Greenland, but provide higher temporal and vertical resolution. Pfeffer and Humphrey (1996) noted that diurnal pulses of energy extended to 20–40 cm in the percolation zone of an outlet glacier on the west coast of Greenland, consistent with the approximately 30 cm depth found here. Kuipers Munneke et al. (2009) also found that SWA was an important component to explain the diurnal cycle of near-surface temperature at Summit Station. Outside of Greenland, Chen et al. (2013) also observed enhanced variability of temperature and gradients near the surface in a seasonal mountain snowpack in winter and spring. Past studies (e.g., Saito et al., 2024) found a tradeoff between latent heat release from refreeze and conduction to move heat deeper into the firn, specifically that conduction moves more energy at higher elevations with less melt. We also observe a tradeoff between conduction and latent heat due to temperature profiles becoming isothermal when melt occurs. However, we find that conduction responds to the warming of latent heat release, particularly near the surface, because surface melt was episodic rather than continuous. The complex near-surface temperature gradients in response to melt and refreeze cause subsurface temperature maxima. High resolution temperature observations are needed to resolve the possible nonlinear temperature gradients in the upper tens of centimeters, which are entirely missed by lower resolution temperature strings.

Our interpretations of the near-surface processes are constrained by our measurements and their respective uncertainties. The upper few centimeters that are most strongly coupled to the surface and atmosphere could also be impacted by wind pumping or ventilation under certain conditions (e.g., Albert and Mcgilvary, 1992; Bartlett and Lehning, 2011) that could also act quickly to produce rapid change in temperature. However, we do not have observations of air movement below the surface to fully explore this process. Temperatures within the upper 20 cm, and particularly in the rapid-response layer, have the largest corrections applied from solar heating of the temperature string (Fig. 2b), which itself depends on the identification of the surface height within the observations. The high correlation and standard deviation near the surface could also be explained by uncertainty in the surface height detection with sensors actually being in the atmosphere. However, the strong correlation between the $T_{\mathrm{skin,rad}}$ and $T_{\mathrm{sfc,string}}$ gives some confidence that the surface is correctly identified.

Another limitation of this study is the fact that the observations only cover two months of data during a year with limited melt. In this dataset melt is episodic. We would expect more or continuous melt to reduce near surface variability in the rapid-response and diurnally-responsive layers as temperature would be limited to 0 °C. Energy transport into the seasonally-responsive layer could increase either through stronger temperature gradients between the isothermal firn above or through percolation of meltwater.

Given such uncertainties, there is still room for improvement. For future observations, temperature profiles should be accompanied by surface height observations as part of the installation to avoid complications of spatial heterogeneity. Co-located SW observations in the subsurface, such as from a light chain or harp (e.g., Katlein et al., 2021), would also improve the solar bias heating correction and provide direct observations of SWA. Improvements could be made to the temperature string installation to limit instrument induced melt. Consideration should also be given to the support used for the temperature strings given the evidence we find of the manufacturer-provided support pole influencing temperature gradients (Fig. C2).

While we attempted to quantify the energy associated with percolation and refreezing of meltwater, uncertainty from density and thermal conductivity estimates limits its interpretation. More frequent, if not continuous, observations of firn density and/or thermal conductivity profiles are needed

to calculate subsurface fluxes with reduced uncertainty to acquire the energy associated with melt and refreezing from residuals, consistent with the conclusion from Van Tiggelen et al. (2024). Improved estimates of subsurface energy fluxes are also crucial for comparing them to atmospheric radiative and turbulent fluxes given that the magnitude of subsurface fluxes at depth can be a similar order of magnitude as the uncertainty in atmospheric fluxes. Higher temporal resolution observations of firn properties would also be useful for studying feedbacks in the subsurface, such as how the formation of ice lenses or depth hoar could interact with temperature gradients and subsurface fluxes (e.g., Colbeck, 1989; Gehl et al., 2025).

Although modeling the subsurface is beyond the scope of this work, future studies would benefit from incorporating firn models. While it is clear observations with high vertical and temporal resolution are necessary for observing and understanding the near-surface firn temperature variability, it remains to be seen if resolving such processes with high-resolution is necessary for modeling the overall seasonal evolution of ice sheets. Observations of firn temperature profiles could be supplemented by models used to quantify energy associated with surface melt and refreeze processes (e.g., Covi et al., 2023). Such analyses are not included in this work due to the complexities of these observations; in particular the advection of meltwater to the temperature string violates the assumption of a closed system used in 1D models (e.g., Charalampidis et al., 2016). Models could also benefit from using the thermodynamic layers to evaluate energy transfer in the near surface firn, ideally with additional observations to ensure statistical robustness.

A natural extension of this work would be to relate the atmospheric fluxes to the firn temperature observations. While we showed the coupling between $T_{\mathrm{skin,rad}}$ and temperature with depth, the atmospheric drivers of $T_{\mathrm{skin,rad}}$ could be further explored. Future work will further investigate the impact of atmospheric variability on the full surface energy budget and subsurface temperatures. Such an analysis will help to quantify the energy related to melt from atmosphere and subsurface perspectives through the surface energy budget that couples them.

Appendix A: Instruments

Details of the instruments used, along with their uncertainties and footprints, are provided in Table A1.

Table A1. Instruments used to measure or derive variables used in study. Unavailable uncertainties are listed as N/A.

Variable (symbol)	Instrument(s)	Uncertainty	Footprint
Broadband up- and downwelling longwave radiation (LWU, LWD)	pyrgeometers; Hukseflux IR-20	LWU: 1 W m^{-2}, LWD: 2.6 W m^{-2}	hemispheric; $\sim$ 5 m circle on surface
Broadband up- and downwelling shortwave radiation (SWU, SWD)	pyranometers; Hukseflux SR-30	3.1 W m^{-2}	hemispheric; $\sim$ 5 m circle on surface
Direct downwelling shortwave radiation	pyranometer; Delta-T SPN1	5 %	hemispheric
Skin temperature ($T_{\mathrm{skin,rad}}$)	derived from broadband radiation measurements	$\sim$ 0.4 °C	$\sim$ 5 m circle on surface
Surface brightness temperature	infrared thermometer (8–14 µm); Apogee	0.14 °C	$\sim$ 2 m circle on surface
Firn temperature (T)	temperature string (2 cm resolution); SAMS Enterprise SIMBA	0.5 °C for $T > -10$ °C; 0.5–2 °C for $T < -10$ °C	vertical column
Firn density (ρ)	manual cutter; capacitance based; American Avalanche Association (2022)	N/A	2 × 2 m plane
Wind speed	3D sonic anemometer; Metek μ-Sonic Cage MP	0.3 m s^{-1}	point measurement
Air temperature (T_{air})	met package; Vaisala PTU307	0.4 °C	point measurement
Melt index	ground penetrating radar (5.4, 7.7 GHz); similar to Brangers et al. (2024) and Brangers et al. (2024)	N/A	vertical column
Surface height, relative	laser sounder; RM Young SNOdar	1–2 cm	point measurement
Surface height, relative	acoustic sounder; Campbell Scientific SR50	1.2 cm	point measurement
Surface height distribution	Open GNSS Research Equipment; Pickell et al. (2025)	2.8 cm	$\sim$ 100 m area

Appendix B: Solar heating correction for skin temperature and upwelling longwave flux

The skin temperature ($T_{\mathrm{skin,rad}}$) was derived using a radiometric method and serves as an independent measure of the surface temperature to validate the temperature string methods. It is calculated from up- and downwelling longwave radiation (LWU, LWD, respectively):

$$T_{\mathrm{skin,rad}} = \left[\frac{\mathrm{LWU} - (1-\varepsilon)\mathrm{LWD}}{\varepsilon\sigma}\right]^{1/4}, \tag{B1}$$

where σ is the Stefan-Boltzmann constant, and ε is snow surface emissivity, assumed to be 0.985 (Warren, 2019, and references therein). Without any corrections, Eq. (B1) produces $T_{\mathrm{skin,rad}}$ values greater than 0 °C (Fig. B1a). These unphysical measurements occur more frequently with greater incident shortwave radiation, which suggests that there is solar heating of the pyrgeometer domes, as has been documented over snow-covered surfaces (e.g., Kuipers Munneke et al., 2009). We assume the bias is due to heating of the downward looking pyrgeometer, i.e., a bias in LWU, because the upward looking pyrgeometer can more efficiently emit excess heat to the atmosphere. Therefore we develop a correction for the upwelling longwave flux and then recalculate $T_{\mathrm{skin,rad}}$ to ensure that the surface energy budget and $T_{\mathrm{skin,rad}}$ are physically consistent.

The magnitude of a $T_{\mathrm{skin,rad}}$ measurement greater than 0 °C is the minimum bias, so we subset the data to calculate a bias correction only for the points we are most confident that the surface is actually melting. This subset includes timesteps when the air temperature is greater than 0 °C, $T_{\mathrm{skin,rad}} \geq 0$ °C, and the GPR melt index (Gallagher et al., 2026a) is ≥ 0.6 (Fig. B1b). Under these conditions, we calculate the bias in longwave flux, ΔLW, as

$$\Delta\mathrm{LW} = \mathrm{LWU} - (1-\varepsilon)\mathrm{LWD} - \varepsilon\sigma T_{\mathrm{skin,rad}}^4, \tag{B2}$$

substituting $T_{\mathrm{skin,rad}} = 273.15$ K. We assume a linear relationship between the longwave bias and upwelling shortwave radiation that is incident on the downward looking pyrgeometer, and use linear least-squares regression to determine the slope and intercept (Fig. B1b). The upwelling flux is corrected at all times, and then $T_{\mathrm{skin,rad}}$ is recalculated.

While this correction is empirical, the results are consistent with physical expectations that $T_{\mathrm{skin,rad}}$ is limited to a maximum of 0 °C. The corrected $T_{\mathrm{skin,rad}}$ also generally agrees with independent infrared brightness temperature observations (Fig. B1c), which are insensitive to solar heating. We estimate the uncertainty in $T_{\mathrm{skin,rad}}$ from uncertainty in emissivity (± 0.015), LWU ($\pm 1\,\mathrm{W\,m^{-2}}$), and LWD ($\pm 2.6\,\mathrm{W\,m^{-2}}$) added in quadrature. The uncertainty estimates in LWU and LWD are from Cox et al. (2023). The uncertainty for upwelling longwave flux increases by $< 0.1\,\mathrm{W\,m^{-2}}$ from this correction, and the uncertainty for the corrected $T_{\mathrm{skin,rad}}$ is ± 0.4 °C.

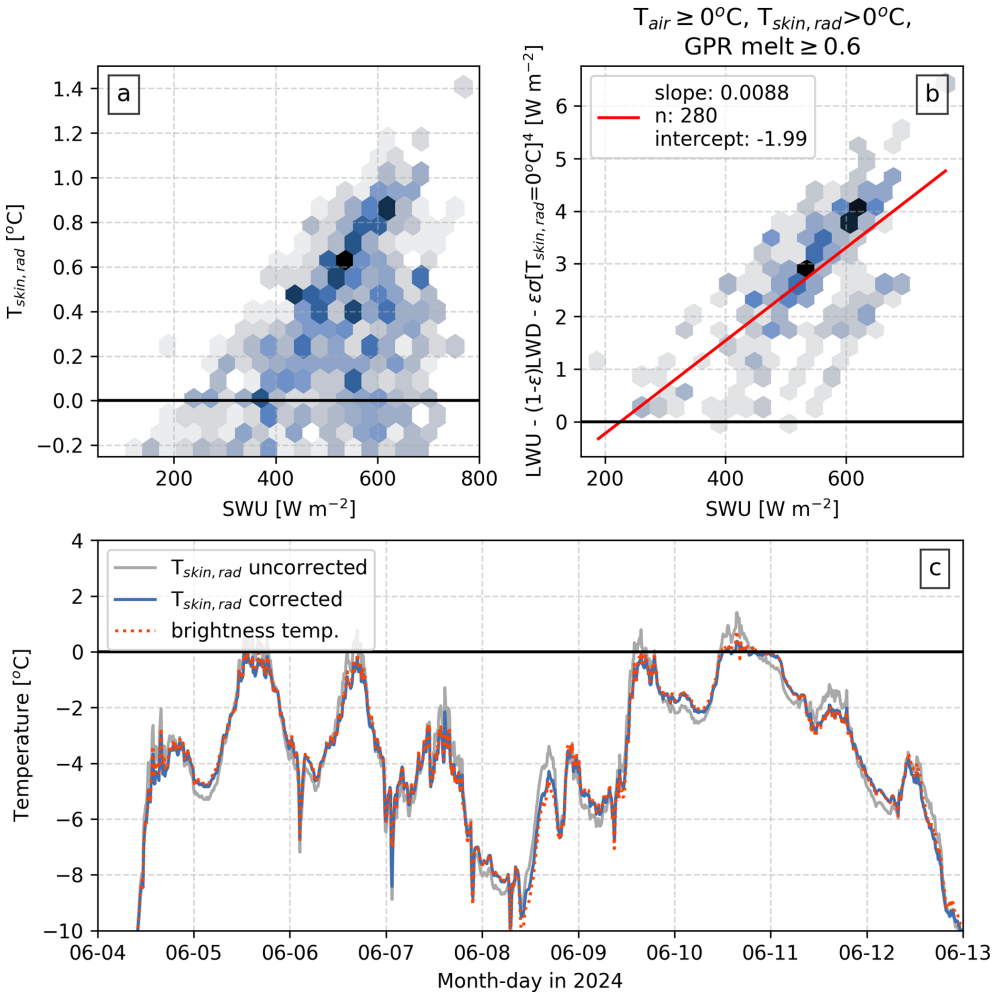


Figure B1. **(a)** Raw skin temperature ($T_{\mathrm{skin,rad}}$) observations plotted against upwelling solar radiation (SWU). **(b)** Regression of longwave flux bias against upwelling shortwave radiation (SWU) used to determine a correction for upwelling longwave radiation (LWU). The y-axis represents the difference between measured LW fluxes and expected longwave emission for a melting surface when $T_{\mathrm{skin,rad}}$ is 0 °C. Only time steps when the air temperature (T_{air}) is at least 0 °C, $T_{\mathrm{skin,rad}}$ is above 0 °C, and the GPR melt index is greater than 0.6 are used for the linear regression (red line). **(c)** Comparisons of uncorrected and corrected $T_{\mathrm{skin,rad}}$ measurements against brightness temperature.

Appendix C: Temperature string height adjustments

To install the temperature string, a vertical hole was drilled in the firn and backfilled with snow after the temperature string was inserted to a depth of ~ 120 cm. The upper meter of the temperature string was mounted to a plastic mount plate secured to an aluminum support pole, and the lower section was looped at the surface then over a supporting piece of wood and into the surface (Fig. C1a, c). This configuration was designed so that the temperature sensors in the firn could be installed vertically yet away from the support pole that protruded into the subsurface, in order to mitigate measurement issues from heating and wicking of meltwater. Additionally, this approach meant that there were multiple measurements from the same string over the lowest part of the atmosphere directly above the surface. This design was chosen with the expectation that there would be net ablation at the site, i.e., the surface would lower over time. As it turned out, there was net accumulation over the season, and the lower temperature string section and the wood support were eventually buried (Fig. C1b).

To provide a consistent temperature profile, we combine the lower section below the support arm and the upper section along the vertical plastic mount plate, effectively removing the looped section of the string. Both sections have sensors at the same heights between 6–58 cm relative to the surface height at installation, but there are differences between temperature sensors at the same height relative to the surface that we attribute to spatial heterogeneity of the snow, differences in thermal capacity of the plastic support compared to the snow, and possible biases in individual sensors (Fig. C2). Over all heights and times, the mean difference in temperature is 0.39 °C with a standard deviation of 1.4 °C and a mean absolute difference of 1.6 °C. Concatenating the lower section and the upper section at a particular height would create artifacts in the vertical temperature and gradients, so an offset is applied to the upper section at and above the height where the two sections are combined. This choice assumes that the lower section is more representative of the firn because it is freestanding.

The offset is calculated and applied at two different heights for different time periods due to surface accumulation. For the first time period, 20 May–27 June, the splice height is +46 cm relative to the surface height at installation, so all firn temperature measurements are from the lower temperature string section because the offset height is above the surface height. This choice eliminates potential discontinuities in vertical profiles. On 27 June there was a large accumulation event that increased the surface height by roughly 25 cm (Fig. C2). After this time the splice height is set to +6 cm, meaning that the upper 50 cm of observations in the snow were from the upper temperature string section. The lower offset height has smaller differences between the upper and lower sections in temperature (Fig. C2e) and vertical temperature gradient (Fig. C2f) compared to near the surface.

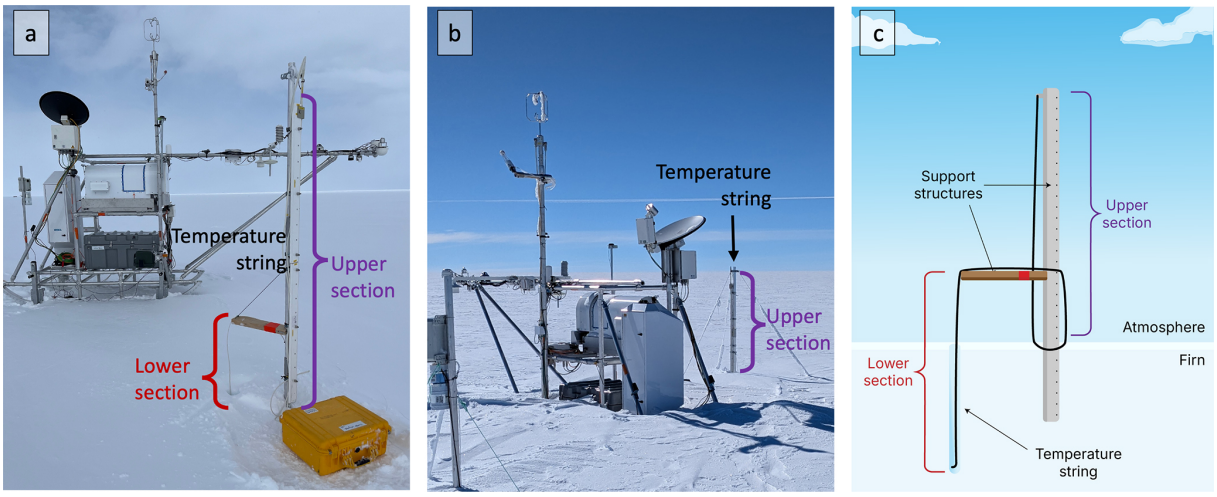


Figure C1. **(a)** Temperature string shortly after installation in May 2024. Photo credit: Matthew Shupe. **(b)** Temperature string during decommissioning in August 2024. Photo credit: Anne Sledd. **(c)** Schematic of temperature string. Credit: Laura Lipuma. The lower section (red) was installed to be freestanding but was buried by fresh accumulation.

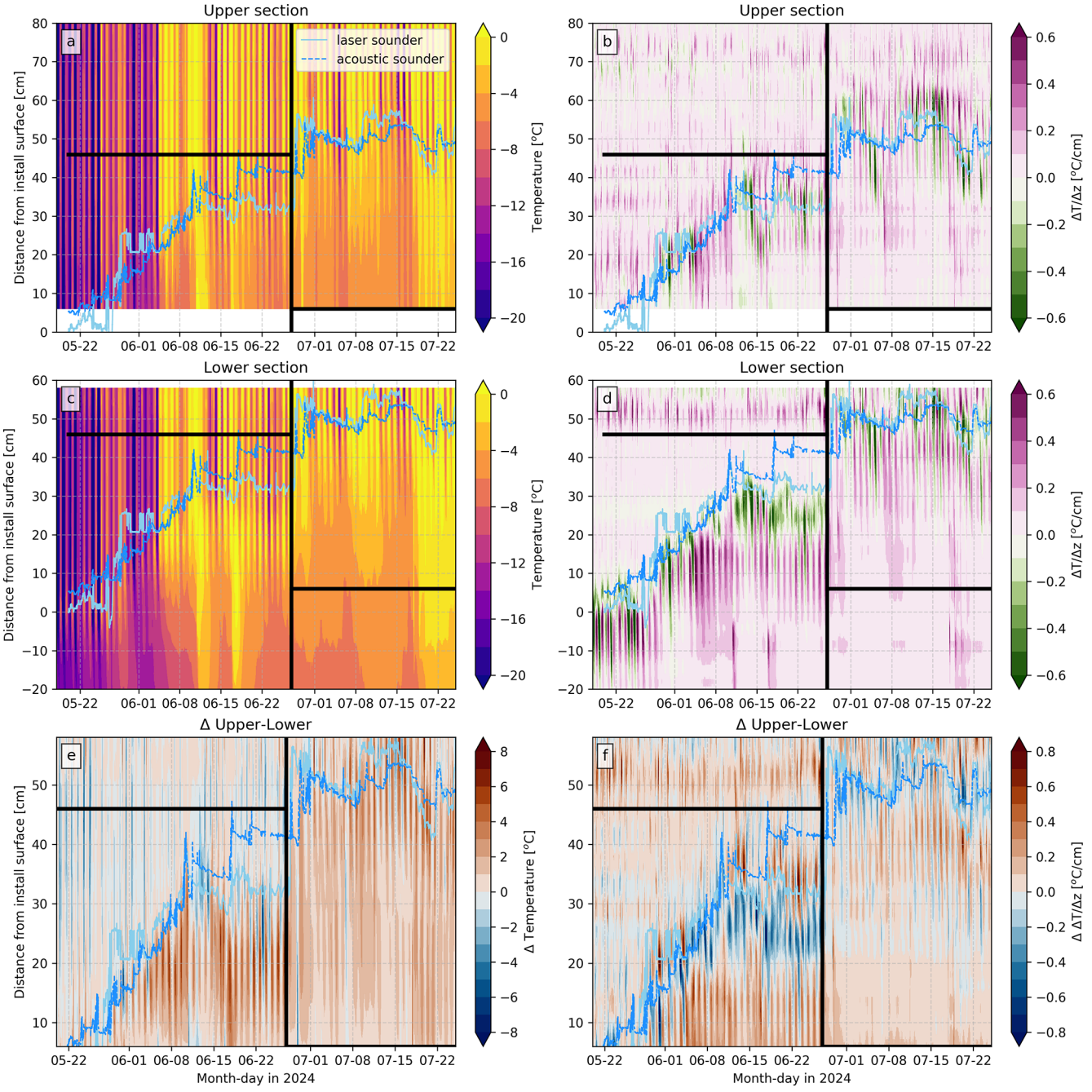


Figure C2. Differences in temperature **(a, c, e)** and vertical temperature gradient ($\Delta T/\Delta z$; **b, d, f**) between upper and lower sections of the temperature string defined in Fig. 1c. The black horizontal lines show the offset height used when concatenating the temperature string. Before 27 June (black vertical line) the offset height is +46 cm, comfortably above the firn surface. After 27 June the offset height is +6 cm, where differences in observed temperature and vertical gradient are smaller than closer to the surface.

Appendix D: Supplemental figures

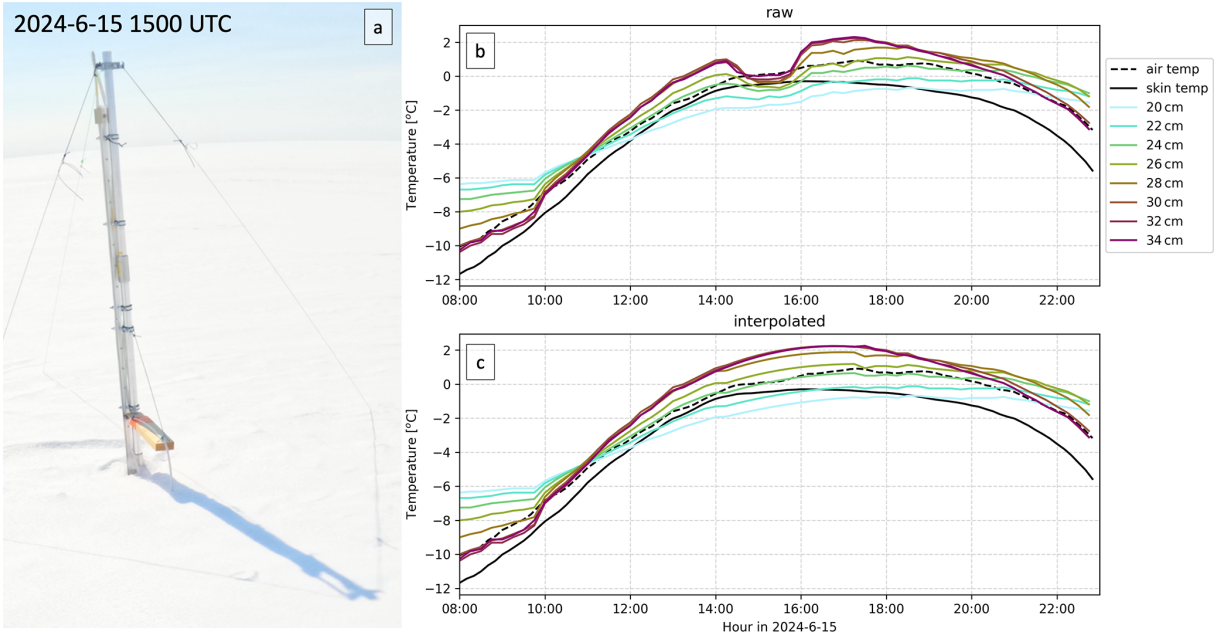


Figure D1. **(a)** Shading of the lower temperature string section, captured by a GoPro camera results in **(b)** lower temperature measurements that disagree with independent air and skin temperature measurements (black dashed and solid lines. **(c)** Suspect data are removed for days when the diffuse fraction is less than 0.5 between 10:00–17:00. The time series is then interpolated using spline fits to fill in missing data.

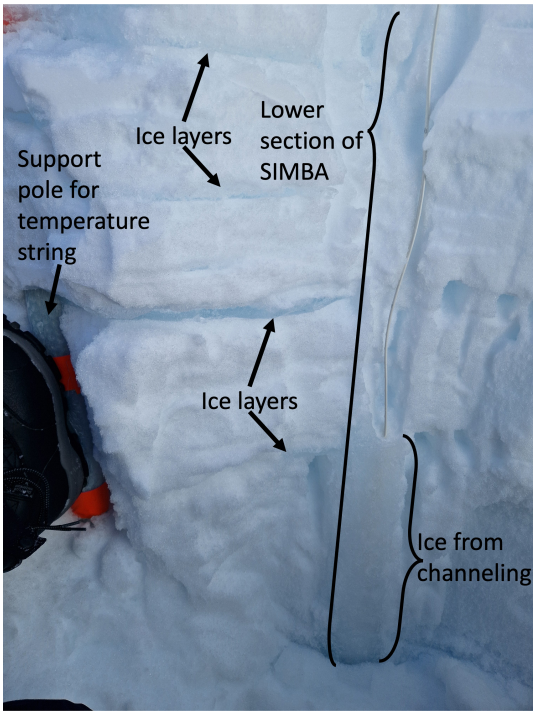


Figure D2. Evidence of channeling down the temperature string support and over to the free standing temperature string below the surface found when removing the temperature string. Additional interpretation provided in the video supplement.

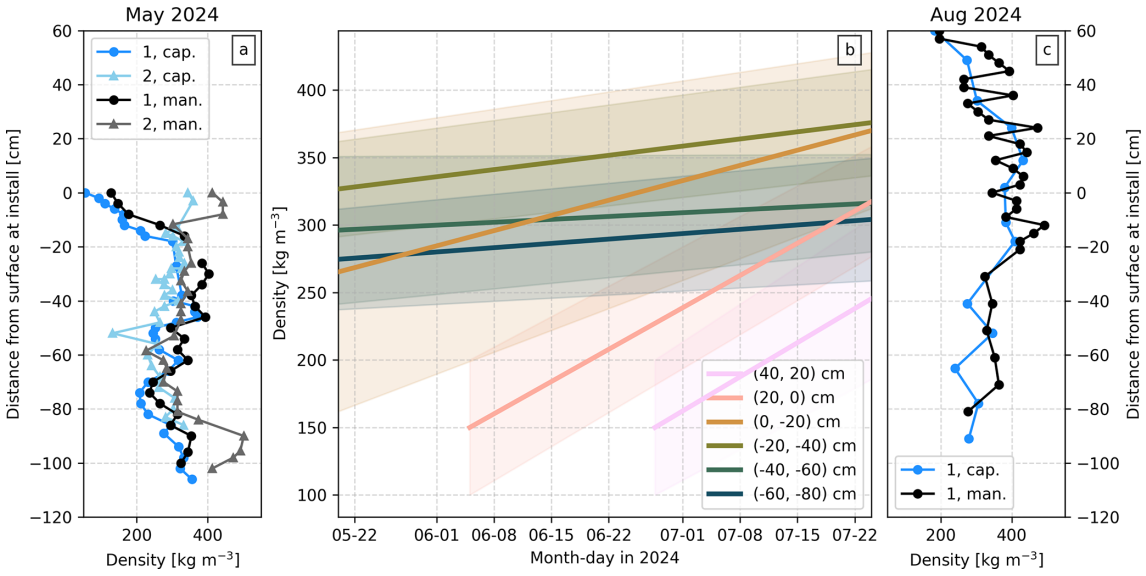


Figure D3. **(a)** and **(c)** show profiles of density measurements using manual (black and grey, "man") and capacitance (blues, "cap") based methods when the instruments were installed **(a)** and decommissioned **(c)**. Different symbols in **(a)** represent two different snowpits (1 or 2). **(b)** The mean density for 20 cm layers linearly interpolated over time, with the shading indicating ± 1 standard deviation. These density estimates are used to calculate internal energy and thermal conductivity for conduction in Figs. 10 and D4.

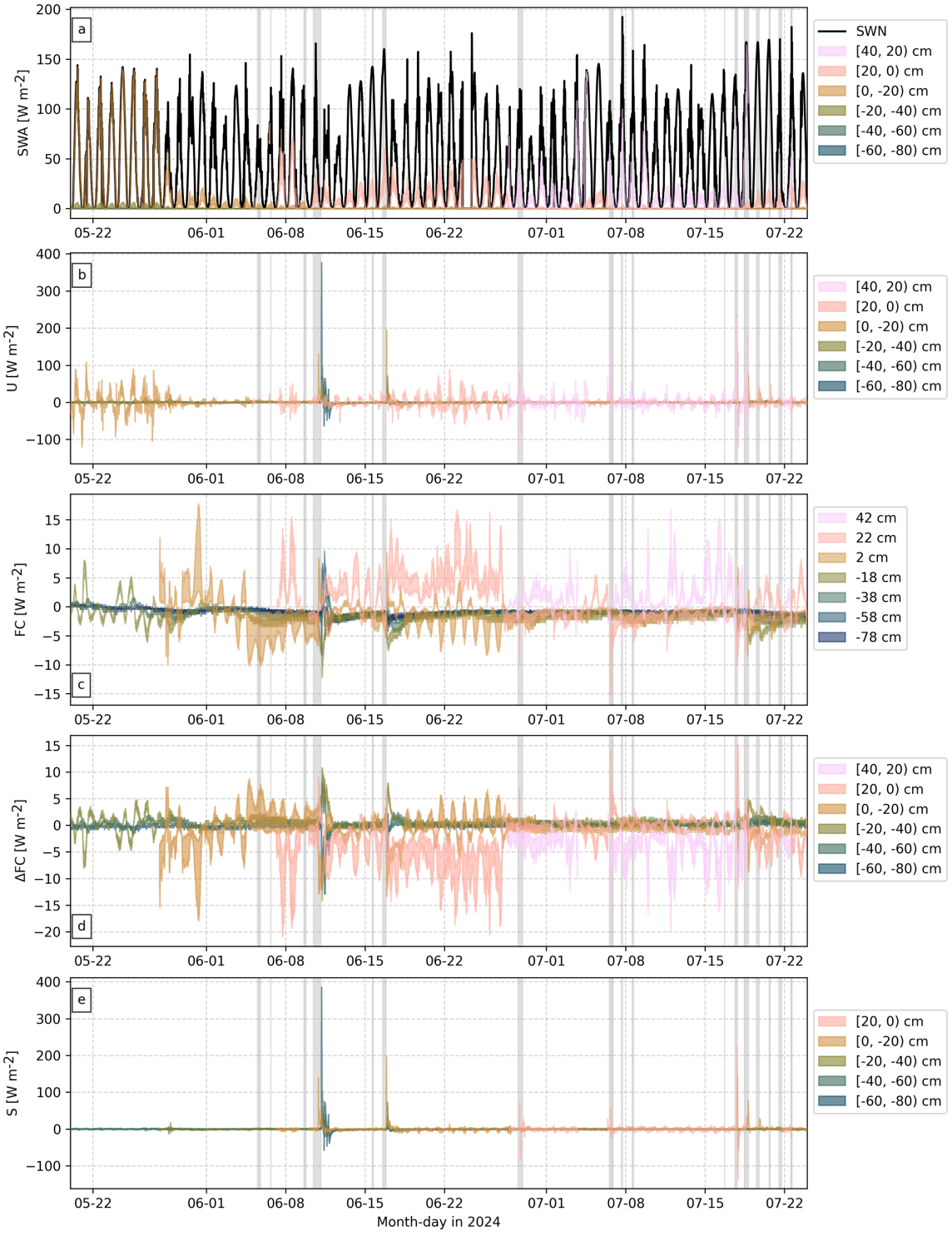


Figure D4. Subsurface fluxes include absorbed solar radiation (SWA) **(a)**, storage or change in internal energy (U) **(b)**, conduction (FC) **(c)**, the net conduction into or out of a layer (ΔFC) **(d)**, and the residual (S) **(e)**. Conduction is calculated at specified levels, and all other variables are calculated over 20 cm layers relative to the initial surface when instruments were installed. Shading around lines for a given layer represents uncertainty due to the range of density measurements, shown in Fig. D3. Vertical gray shading indicates times when $T_{\text{skin,rad}} \sim 0\,^{\circ}\text{C}$.

Data availability. Snow pit observations are available from Town et al. (2026) (https://catalogue.ceda.ac.uk/uuid/aef72bc18a244465a721646babf3018a/, last access: 26 February 2026). Temperature string data are available from Sledd et al. (2026) (https://doi.org/10.18739/A2RJ48X3W). GPR data are available from Hawley et al. (2026) (https://doi.org/10.18739/A2PK0743C). Radiative flux and meteorological observations are available from Gallagher et al. (2026b) (https://doi.org/10.18739/A21V5BG69).

Video supplement. The video supplement provides interpretation of ice layers around the temperature string (referred to as SIMBA and SIMBA chain) during decommissioning of instrument, shown in Fig. D2 (https://doi.org/10.5281/zenodo.19360813, Guy and Sledd, 2026).

Author contributions. AS, MRG, MDS contributed to conception and design. AS, MRG, MDS, CJC, RH, HG, HPM, CP, MST, VPW contributed to analysis and interpretation of data. AS, MRG, MDS, RH, HG, CP, MST, VPW, CH, HPM, AM, RN, EO, DP contributed to data acquisition and curation. AS prepared the manuscript with contributions from MRG, MDS, CJC, RH, HG, HPM, RN, CP, MST, VPW.

Competing interests. The contact author has declared that none of the authors has any competing interests.

Disclaimer. Publisher's note: Copernicus Publications remains neutral with regard to jurisdictional claims made in the text, published maps, institutional affiliations, or any other geographical representation in this paper. The authors bear the ultimate responsibility for providing appropriate place names. Views expressed in the text are those of the authors and do not necessarily reflect the views of the publisher.

Acknowledgements. The scientific colour maps vik, hawaii, bam, batlow, navia, bamako, devon, and lapaz (Crameri, 2018) are used in this study to prevent visual distortion of the data and exclusion of readers with colour-vision deficiencies (Crameri et al., 2020). The authors additionally thank Darren Jackson and the two anonymous referees for feedback on the manuscript.

Financial support. This research has been supported by the National Science Foundation, Directorate for Geosciences (grant nos. 2137091, 2137152, 2137098, and 2137083), the National Centre for Earth Observation (grant no. NE/X002403/1), and the NOAA Research (grant no. NA22OAR4320151).

Review statement. This paper was edited by Michiel van den Broeke and reviewed by two anonymous referees.

References

Albert, M. R. and Mcgilvary, W. R.: Thermal effects due to air flow and vapor transport in dry snow, J. Glaciol., 38, 273–281, https://doi.org/10.3189/S0022143000003683, 1992.

American Avalanche Association: Snow, Weather, and Avalanches: Observation Guidelines for Avalanche Programs in the United States, 4th edn., American Avalanche Association, Denver Colorado, 10–47, 2022.

Bartlett, S. J. and Lehning, M.: A theoretical assessment of heat transfer by ventilation in homogeneous snowpacks, Water Resour. Res., 47, 2010WR010008, https://doi.org/10.1029/2010WR010008, 2011.

Bohren, C. F. and Barkstrom, B. R.: Theory of the optical properties of snow, J. Geophys. Res., 79, 4527–4535, https://doi.org/10.1029/JC079i030p04527, 1974.

Brandt, R. E. and Warren, S. G.: Solar-heating rates and temperature profiles in Antarctic snow and ice, J. Glaciol., 39, 99–110, https://doi.org/10.3189/S0022143000015756, 1993.

Brangers, I., Marshall, H.-P., De Lannoy, G., Dunmire, D., Mätzler, C., and Lievens, H.: Tower-based C-band radar measurements of an alpine snowpack, The Cryosphere, 18, 3177–3193, https://doi.org/10.5194/tc-18-3177-2024, 2024.

Brangers, I., De Lannoy, G., Marshall, H.-P., Dunmire, D., Bonnell, R., Cox, B., Cappelle, J., Baxter, W. B., and Lievens, H.: C-Band Radar Measurements in a Snow-Covered Boreal Forest Environment, IEEE Geosci. Remote Sens. Lett., 22, 1–5, 2024.

Calonne, N., Milliancourt, L., Burr, A., Philip, A., Martin, C. L., Flin, F., and Geindreau, C.: Thermal conductivity of snow, firn, and porous ice from 3-D image-based computations, Geophys. Res. Lett., 46, 13079–13089, 2019.

Charalampidis, C., Van As, D., Colgan, W. T., Fausto, R. S., Macferrin, M., and Machguth, H.: Thermal tracing of retained meltwater in the lower accumulation area of the Southwestern Greenland ice sheet, Ann. Glaciol., 57, 1–10, https://doi.org/10.1017/aog.2016.2, 2016.

Chen, X., Wei, W., and Liu, M.: Characteristics of temperature variation in seasonal snow in the Western Tianshan Mountains, China, Meteorol. Appl., 20, 457–465, 2013.

Colbeck, S.: Air movement in snow due to windpumping, J. Glaciol., 35, 209–213, 1989.

Colbeck, S.: Model of wind pumping for layered snow, J. Glaciol., 43, 60–65, 1997.

Colgan, W., Pedersen, A., Binder, D., Machguth, H., Abermann, J., and Jayred, M.: Initial field activities of the camp century climate monitoring programme in Greenland, GEUS Bull., 41, 75–78, 2018.

Covi, F., Hock, R., and Reijmer, C. H.: Challenges in modeling the energy balance and melt in the percolation zone of the Greenland ice sheet, J. Glaciol., 69, 164–178, https://doi.org/10.1017/jog.2022.54, 2023.

Cox, C. J., Gallagher, M. R., Shupe, M. D., Persson, P. O. G., Solomon, A., Fairall, C. W., Ayers, T., Blomquist, B., Brooks, I. M., Costa, D., Grachev, A., Gottas, D., Hutchings, J. K., Kutchenreiter, M., Leach, J., Morris, S. M., Morris, V., Osborn, J., Pezoa, S., Preußer, A., Riihimaki, L. D., and Uttal, T.: Continuous observations of the surface energy budget and meteorology over the Arctic sea ice during MOSAiC, Sci. Data, 10, 519, https://doi.org/10.1038/s41597-023-02415-5, 2023.

Crameri, F.: Scientific colour maps, Zenodo, https://doi.org/10.5281/zenodo.1243862, 2018.

Crameri, F., Shephard, G. E., and Heron, P. J.: The misuse of colour in science communication, Nat. Commun., 11, 5444, https://doi.org/10.1038/s41467-020-19160-7, 2020.

Dadic, R., Schneebeli, M., Lehning, M., Hutterli, M. A., and Ohmura, A.: Impact of the microstructure of snow on its temperature: A model validation with measurements from Summit, Greenland, J. Geophys. Res.-Atmos., 113, 2007JD009562, https://doi.org/10.1029/2007JD009562, 2008.

Denoth, A.: Snow dielectric measurements, Adv. Space Res., 9, 233–243, 1989.

Fausto, R. S., Van As, D., Mankoff, K. D., Vandecrux, B., Citterio, M., Ahlstrøm, A. P., Andersen, S. B., Colgan, W., Karlsson, N. B., Kjeldsen, K. K., Korsgaard, N. J., Larsen, S. H., Nielsen, S., Pedersen, A. ø., Shields, C. L., Solgaard, A. M., and Box, J. E.: Programme for Monitoring of the Greenland Ice Sheet (PROMICE) automatic weather station data, Earth Syst. Sci. Data, 13, 3819–3845, https://doi.org/10.5194/essd-13-3819-2021, 2021.

Gallagher, M., Shupe, M., Walden, V., Sledd, A., Cox, C., Guy, H.; Pettersen, C., Martin, A., Neely, R., Hawley, R., Town, M., Marshall, H.-P., Pickell, D., Mattingly, K., Vandecrux, B., Mottram, R., Clemens-Sewall, D., Olson, E., and Hebson, C.: How Greenland melts under cloudy and clear skies, Nature, Earth-ArXiv, https://doi.org/10.31223/X5J236, 2026a.

Gallagher, M., Shupe, M., Sledd, A., and Cox, C.: Atmospheric Surface Flux Station measurements near Raven Camp, Greenland in Summer 2024, Level 2 data, Arctic Data Center [data set], https://doi.org/10.18739/A21V5BG69, 2026b.

Gehl, K. L., Harper, J. T., and Humphrey, N. F.: Kinetic grain growth in firn induced by meltwater infiltration on the Greenland Ice Sheet, The Cryosphere, 19, 6791–6805, https://doi.org/10.5194/tc-19-6791-2025, 2025.

Guy, H. and Sledd, A.: Video supplement for "Summer subsurface temperature variability in the percolation zone of southwest Greenland: high resolution observations of the top meter of firn", Zenodo [video], https://doi.org/10.5281/zenodo.19360814, 2026.

Guy, H., Neely III, R., and Brooks, I.: ICECAPS-ACE: snow-air transition temperatures taken at Summit Station Greenland, https://catalogue.ceda.ac.uk/uuid/6db2c027914d4f23bd42409e7aaad3b1/ (last access: 7 March 2026), 2023.

Hawley, R., Marshall, H. P., and Wilson, L.: Stationary Ground Penetrating Radar traces from the percolation zone of the Greenland Ice Sheet (summer 2024), Arctic Data Center [data set], https://doi.org/10.18739/A2PK0743C, 2026.

Hills, B. H., Harper, J. T., Meierbachtol, T. W., Johnson, J. V., Humphrey, N. F., and Wright, P. J.: Processes influencing heat transfer in the near-surface ice of Greenland's ablation zone, The Cryosphere, 12, 3215–3227, https://doi.org/10.5194/tc-12-3215-2018, 2018.

Humphrey, N. F., Harper, J. T., and Pfeffer, W. T.: Thermal tracking of meltwater retention in Greenland's accumulation area, J. Geophys. Res.-Earth, 117, 2011JF002083, https://doi.org/10.1029/2011JF002083, 2012.

Katlein, C., Valcic, L., Lambert-Girard, S., and Hoppmann, M.: New insights into radiative transfer within sea ice derived from autonomous optical propagation measurements, The Cryosphere, 15, 183–198, https://doi.org/10.5194/tc-15-183-2021, 2021.

Kuipers Munneke, P., Van Den Broeke, M. R., Reijmer, C. H., Helsen, M. M., Boot, W., Schneebeli, M., and Steffen, K.: The role of radiation penetration in the energy budget of the snowpack at Summit, Greenland, The Cryosphere, 3, 155–165, https://doi.org/10.5194/tc-3-155-2009, 2009.

McGrath, D., Colgan, W., Bayou, N., Muto, A., and Steffen, K.: Recent warming at Summit, Greenland: Global context and implications, Geophys. Res. Lett., 40, 2091–2096, https://doi.org/10.1002/grl.50456, 2013.

Mellor, M.: Engineering properties of snow, J. Glaciol., 19, 15–66, 1977.

Mottram, R., B. Simonsen, S., Høyer Svendsen, S., Barletta, V. R., Sandberg Sørensen, L., Nagler, T., Wuite, J., Groh, A., Horwath, M., Rosier, J., Solgaard, A., Hvidberg, C. S., and Forsberg, R.: An Integrated View of Greenland Ice Sheet Mass Changes Based on Models and Satellite Observations, Remote Sens., 11, 1407, https://doi.org/10.3390/rs11121407, 2019.

Perovich, D. K.: Light reflection and transmission by a temperate snow cover, J. Glaciol., 53, 201–210, 2007.

Persson, P. O. G.: Onset and end of the summer melt season over sea ice: Thermal structure and surface energy perspective from SHEBA, Clim. Dynam., 39, 1349–1371, 2012.

Pfeffer, W. T. and Humphrey, N. F.: Determination of timing and location of water movement and ice-layer formation by temperature measurements in sub-freezing snow, J. Glaciol., 42, 292–304, https://doi.org/10.3189/S0022143000004159, 1996.

Pickell, D. J., Hawley, R. L., and LeWinter, A.: Spatiotemporal patterns of accumulation and surface roughness in interior Greenland with a GNSS-IR network, The Cryosphere, 19, 1013–1029, https://doi.org/10.5194/tc-19-1013-2025, 2025.

Poinar, K., Box, J. E., Mote, T. L., Fettweis, X., Loomis, B. D., Smith, B. E., Medley, B., Mankoff, K. D., Askjaer, T. G., Fausto, R. S., and Tedesco, M.: 2025: Greenland Ice Sheet, "State of the Climate in 2024", Bull. Am. Meteorol., 106, S328–S331, 2025.

Saito, J., Harper, J., and Humphrey, N.: Uptake and Transfer of Heat Within the Firn Layer of Greenland Ice Sheet's Percolation Zone, J. Geophys. Res.-Earth, 129, e2024JF007667, https://doi.org/10.1029/2024JF007667, 2024.

Samimi, S., Marshall, S. J., and MacFerrin, M.: Meltwater Penetration Through Temperate Ice Layers in the Percolation Zone at DYE-2, Greenland Ice Sheet, Geophys. Res. Lett., 47, e2020GL089211, https://doi.org/10.1029/2020GL089211, 2020.

Samimi, S., Marshall, S. J., Vandecrux, B., and MacFerrin, M.: Time-Domain Reflectometry Measurements and Modeling of Firn Meltwater Infiltration at DYE-2, Greenland, J. Geophys. Res.-Earth, 126, e2021JF006295, https://doi.org/10.1029/2021JF006295, 2021.

Shupe, M. D., Turner, D. D., Walden, V. P., Bennartz, R., Cadeddu, M. P., Castellani, B. B., Cox, C. J., Hudak, D. R., Kulie, M. S., Miller, N. B., Neely, R. R., Neff, W. D., and Rowe, P. M.: High and Dry: New Observations of Tropospheric and Cloud Properties above the Greenland Ice Sheet, Bull. Am. Meteorol. Soc., 94, 169–186, https://doi.org/10.1175/BAMS-D-11-00249.1, 2013.

Sledd, A., Shupe, M. D., Solomon, A., Cox, C. J., Perovich, D., and Lei, R.: Snow thermal conductivity and conductive flux in the Central Arctic: Estimates from observations

and implications for models, Elem. Sci. Anth., 12, 00086, https://doi.org/10.1525/elementa.2023.00086, 2024.

Sledd, A., Gallagher, M., and Shupe, M.: Firn temperature profiles near Raven Camp, Greenland in Summer 2024, raw and processed data, Arctic Data Center [data set], https://doi.org/10.18739/A2RJ48X3W, 2026.

Tedstone, A. J. and Machguth, H.: Increasing surface runoff from Greenland's firn areas, Nat. Clim. Change, 12, 672–676, https://doi.org/10.1038/s41558-022-01371-z, 2022.

The IMBIE Team: Mass balance of the Greenland Ice Sheet from 1992 to 2018, Nature, 579, 233–239, https://doi.org/10.1038/s41586-019-1855-2, 2020.

Town, M., Walden, V., Martin, A., Guy, H., Sledd, A., Olsen, E., Shupe, M., Gallagher, M., Hebson, C., and Neely III, R.: ICECAPS-MELT: Manual and Instrumented Snow Property Measurements at Camp Raven, Southwest Greenland (May and August 2024), https://catalogue.ceda.ac.uk/uuid/aef72bc18a244465a721646babf3018a/ (last access: 26 February 2026), 2026.

Van Angelen, J. H., Van Den Broeke, M. R., Wouters, B., and Lenaerts, J. T. M.: Contemporary (1960–2012) Evolution of the Climate and Surface Mass Balance of the Greenland Ice Sheet, Surv. Geophys., 35, 1155–1174, https://doi.org/10.1007/s10712-013-9261-z, 2014.

Van Den Broeke, M. R., Smeets, C. J. P. P., and Van De Wal, R. S. W.: The seasonal cycle and interannual variability of surface energy balance and melt in the ablation zone of the west Greenland ice sheet, The Cryosphere, 5, 377–390, https://doi.org/10.5194/tc-5-377-2011, 2011.

Van Den Broeke, M. R., Enderlin, E. M., Howat, I. M., Kuipers Munneke, P., Noël, B. P. Y., Van De Berg, W. J., Van Meijgaard, E., and Wouters, B.: On the recent contribution of the Greenland ice sheet to sea level change, The Cryosphere, 10, 1933–1946, https://doi.org/10.5194/tc-10-1933-2016, 2016.

Van Tiggelen, M., Smeets, P. C. J. P., Reijmer, C. H., Van As, D., Box, J. E., Fausto, R. S., Khan, S. A., Rignot, E., and Van Den Broeke, M. R.: Surface energy balance closure over melting snow and ice from in situ measurements on the Greenland ice sheet, J. Glaciol., 70, e82, https://doi.org/10.1017/jog.2024.68, 2024.

Vandecrux, B., Fausto, R. S., Langen, P. L., Van As, D., MacFerrin, M., Colgan, W. T., Ingeman-Nielsen, T., Steffen, K., Jensen, N. S., Møller, M. T., and Box, J. E.: Drivers of Firn Density on the Greenland Ice Sheet Revealed by Weather Station Observations and Modeling, J. Geophys. Res.-Earth, 123, 2563–2576, https://doi.org/10.1029/2017JF004597, 2018.

Warren, S. G.: Optical properties of snow, Rev. Geophys., 20, 67–89, 1982.

Warren, S. G.: Optical properties of ice and snow, Philos. T. R. Soc. A, 377, https://doi.org/10.1098/rsta.2018.0161, 2019.

Wolfsperger, F., Geisser, M., Ziegler, S., and Löwe, H.: A new handheld capacitive sensor to measure snow density and liquid water content, in: Proceedings of the International Snow Science Workshop 2023, Bend, Oregon, USA, 1532–1536, https://arc.lib.montana.edu/snow-science/item/3092 (last access: 3 November 2026), 2023.

Zheng, M., Ralph, F. M., Tallapragada, V., Wilson, A. M., Babbitt, S. H., Bartlett, S. M., Cao, B., Centurioni, L., Cordeira, J. M., Davis, C., Delle Monache, L., Doyle, J. D., Elless, T. J., Feuer, S., Haase, J. S., Hathaway, N., Hutchinson, T., Iniguez, P., Kawzenuk, B., Knappe, E., Lavers, D. A., Lundry, A., Michaelis, A., Pappenberger, F., Reynolds, C. A., Rickert, R., Roj, S., Rutz, J. J., Subramanian, A. C., Torn, R. D., Wang, J., Wu, K., and Wu, X.: Atmospheric River Reconnaissance: Mission Planning, Execution, and Incorporation of Operational and Science Objectives, Bull. Am. Meteorol. Soc., 106, E2243–E2275, https://doi.org/10.1175/BAMS-D-24-0160.1, 2025.

Zuo, G., Dou, Y., and Lei, R.: Discrimination algorithm and procedure of snow depth and sea ice thickness determination using measurements of the vertical ice temperature profile by the ice-tethered buoys, Sensors, 18, 4162, https://doi.org/10.3390/s18124162, 2018.